UC Berkeley
UC Berkeley Previously Published Works

Title

Estimating fluid-induced stress change from observed deformation

Permalink

Journal

ISSN

Authors

Vasco, DW
Harness, Paul
Pride, Steve
et al.

Publication Date

DOI

Peer reviewed

Estimating fluid-induced stress change from observed deformation

D.W. Vasco,[1] Paul Harness,[2] Steve Pride[1] and Mike Hoversten[3]

[1] *Lawrence Berkeley Laboratory, University of California, Berkeley, CA 94720, USA. E-mail: dwvasco@lbl.gov*
[2] *Chevron North America Exploration and Production, Bakersfield, CA 93311, USA*
[3] *Chevron Energy Technology Company, San Ramon, CA 94583, USA*

SUMMARY

Observed deformation is sensitive to a changing stress field within the Earth. However, there are several impediments to a direct inversion of geodetic measurements for changes in stress. Estimating six independent components of stress change from a smaller number of displacement or strain components is inherently non-unique. The reliance upon surface measurements leads to a loss of resolution, due to the attenuation of higher spatial frequencies in the displacement field with distance from a source. We adopt a technique suited to the estimation of stress changes due to the injection and/or withdrawal of fluids at depth. In this approach the surface displacement data provides an estimate of the volume change responsible for the deformation, rather than stress changes themselves. The inversion for volume change is constrained by the fluid fluxes into and out of the reservoir. The distribution of volume change is used to calculate the displacements in the region above the reservoir. Estimates of stress change follow from differentiating the displacement field in conjunction with a geomechanical model of the overburden. We apply the technique to Interferometric Synthetic Aperture Radar (InSAR) observations gathered over a petroleum reservoir in the San Joaquin Valley of California. An analysis of the InSAR range changes reveals that the stress field in the overburden varies rapidly both in space and in time. The inferred stress variations are found to be compatible with the documented failure of a well in the field.

Key words: Inverse theory; Satellite geodesy; Transient deformation; Radar interferometry; Geomechanics.

1 INTRODUCTION

Stress changes associated with fluid injection and withdrawal are important for several reasons. Knowledge of stress change is important in the context of understanding, and perhaps mitigating, well-bore failure. With adequate insight into the effects of injection and withdrawal on the subsurface, one can balance the net fluid changes at depth, in order to minimize the associated stress alterations. Stress changes influence the growth of fractures and may alter the flow properties of existing fractures and faults, by causing those in a particular orientation to close and others to slip and dilate. For these reasons alone, it is important to understand the evolution of stress, in both space and time, due to fluid injection and production.

Because of its importance, numerous techniques have been developed for measuring or estimating the stress field within the Earth (Zang & Stephansson 2010). The most direct techniques take advantage of boreholes, perturbing the conditions in the borehole and recording the induced strain, or the necessary stress, to achieve a new equilibrium. Such techniques include step-rate tests, overcoring, hydraulic tests on pre-existing fractures (HTPF), the analysis of borehole breakouts and strain recovery, as well as core-disc meth-

ods on drill cores (Ljunggren *et al.* 2003). While borehole-based methods are generally the most accurate, they have the distinct disadvantage of being restricted to well bores. Furthermore, the tests can be time consuming and many tests may be required to obtain estimates of the principle stresses and their orientations.

An alternative approach, one that provides estimates away from boreholes, relies on stress-induced anisotropy and associated velocity changes (Crampin 1978; Bakulin & Protosenya 1982; Leary *et al.* 1990; Mavko *et al.* 1995; Sinha & Kostek 1996; Johnson & Rasolofosaon 1996; Sarkar *et al.* 2003; Prioul *et al.* 2004; Shapiro & Kaselow 2005; Gurevich *et al.* 2011). This indirect technique relies on an inversion of seismic observations. An added complication arises because most materials in the Earth contain pre-existing structural anisotropy, requiring laboratory measurements from core samples to obtain the natural anisotropy in the unstressed state. Because stress-induced anisotropy contains coefficients that depend on the stress field, and hence on the strain, the theory is fundamentally nonlinear. The nonlinear stress–strain relationship is specified by a large number of anisotropy parameters and related coefficients. In order to characterize this relationship and to determine the parameters, multicomponent data must be gathered in many directions in order to estimate the stress. To our knowledge, the approach

has only been applied in the laboratory (Thurston & Brugger 1964; Johnson & Rasolofosaon 1996; Sarkar *et al.* 2003; Prioul *et al.* 2004; Shapiro & Kaselow 2005; Gurevich *et al.* 2011) and has never been attempted in the field.

Stress estimates based upon seismic source inversions also provide information about the spatial and temporal variation of the stress field in the Earth. Early methods relied upon first motion data and event focal methods to estimates gross features of the stress field (Gephart & Forsyth 1984; Michael 1984; Angelier 2002; Hardebeck & Michael 2006; Arnold & Townend 2007), primarily the directions of the principle stresses and their relative magnitudes (Hardebeck & Hauksson 2001). The approach has been modified to utilize full waveforms and the centroid moment tensors of seismic events in order to estimate the 3-D variations of the stress field (Terakawa & Matsu'ura 2008). One limitation of this approach is that estimates are only available where and when seismic events occur. Furthermore, at the field scale, events may not occur frequently enough to provide adequate temporal resolution of a changing stress field.

Geodetic observations provide another set of data that are sensitive to stress variations within the Earth. Some aspects of geodetic data, such as generally frequent temporal sampling, are advantageous. Certain data types, such as Interferometric Synthetic Aperture Radar (InSAR) provide fine spatial sampling as well (Ferretti 2014). Therefore, it seems sensible to use geodetic data to infer stress changes within the Earth and over time. However, there are aspects of such data that limit their usefulness. For example, most observations are gathered at the surface of the Earth and the spatial resolution provided by geodetic data decreases strongly with depth. Techniques such as InSAR usually provide a single component of displacement, meaning that any inverse problem involving the estimation of six independent components of the stress tensor will be severely under-determined. Here, we describe an approach for estimating stress changes associated with fluid injection and withdrawal, whereby the stress changes are not sought directly. Rather, we invert the observations for volumetric changes associated with the fluid fluxes. The estimated volume changes are then used to calculate, in a forward sense, the displacements in the overburden. With the displacement field in hand, and assuming well characterized elastic behaviour in the overburden over the period of interest, the calculated stress changes follow from a straight-forward differentiation. We illustrate the approach by an application to InSAR data gathered over an oil field in central California.

2 METHODOLOGY

Our approach is based upon the assumption that the stress changes are primarily the result of fluid fluxes. Specifically, injected or produced fluid volumes lead to changes in fluid pressure at depth, driving volumetric changes in the region surrounding the reservoir. The model consists of two regions: the reservoir, where fluid injection and withdrawal are active, and the overburden where fluid volume changes may be neglected. The reservoir is a source region that may behave in a complicated, inelastic fashion, while the overburden is assumed to behave elastically, at least over monthly time intervals.

The procedure involves three main steps that will be discussed in some detail in this section. First, we invert the observed range change for the distribution of volume change within the reservoir. The inversion is constrained by a given set of fluid fluxes into and out of the grid blocks of the reservoir model. Second, we use the reservoir volume changes to calculate the displacement field

throughout the overburden. Third, we compute the spatial derivatives of the displacements field and use them to estimate the stress changes at depth. For an elastic medium each step is linear, leading to a linear estimator for the stresses. Thus, a formal linear model assessment may accompany the estimates of stress change. From these three steps one observes the importance of accurate estimates of the geomechanical properties of the overburden in the calculations. The properties are used in both the inverse problem, whereby we estimate the reservoir volume changes, and in the forward calculation of the displacements and stresses. Thus, it is critical to have a well constrained overburden model in order to provide reliable estimates of stress changes. In our application, the properties of the overburden are constrained by numerous logged wells in the region.

2.1 Inverting for the fluid-induced volume change

2.1.1 The forward problem

We suppose that deformation in the region of interest is driven by the injection and withdrawal of fluids. The fluid flux produces a fluid pressure change, leading to a fractional volume change v_f of the solid material. It is assumed that the overburden behaves elastically over the time interval between surveys, roughly one month for the field case considered below. The equation governing the quasi-static deformation of an elastic body is

$$\frac{\partial}{\partial x_j} \left[\mu \left(\frac{\partial u_i}{\partial x_j} + \frac{\partial u_j}{\partial x_i} \right) + \lambda \frac{\partial u_k}{\partial x_k} \delta_{ij} \right] = \frac{\partial}{\partial x_j} [K_u v_f] \delta_{ij} \qquad (1)$$

where $\mu(\mathbf{x})$ is the shear modulus, $\lambda(\mathbf{x})$ is the Lame parameter, and δ_{ij} is the Kronecker delta function which is 1 when i equals j and zero otherwise (Fung 1969). The quantity K_u is the bulk modulus. We adopt the convention of Einstein in which one sums over repeated indices. The volume change v_f occurs on the right-hand side of eq. (1), as a source term. This means that the inverse problem for v_f is linear for a known elastic overburden model. A Green's function for the governing equation is a solution corresponding to the case in which the right-hand side is a Dirac-delta or impulse function (Stakgold 1979). Given a suitable Green's function, $g_i(\mathbf{x}, \zeta)$, we can take advantage of the linearity of the problem and make use of the integral representation of the general solution of eq. (1) (Aki & Richards 1980)

$$u_i(\mathbf{x}, t) = \int_V v_f(\zeta, t) g_i(\mathbf{x}, \zeta) dV, \qquad (2)$$

where ζ denotes the coordinates within the reservoir volume V.

For practical forward and inverse calculations we must turn to a discrete representation of the volume change within the reservoir. In the discrete version of eq. (2), we represent the reservoir volume by a set of N non-intersecting rectangular cells or grid blocks. Each grid block in the reservoir model may undergo a distinct volume change. Because the details were presented in Vasco *et al.* (1988, 2000, 2002b; Vasco & Ferretti 2005; Vasco *et al.* 2010), we only need to present the resulting equations. Given M observation points $\mathbf{x}_j$, the discrete version of eq. (2) is

$$u_i(\mathbf{x}_j, t) = \sum_{n=1}^{N} G^n_{\ i}(\mathbf{x}_j) v_n = \mathbf{G}_i(\mathbf{x}_j) \cdot \mathbf{v}(t), \qquad (3)$$

where v_n is the average volume change for grid block n, and $\mathbf{G}_i(\mathbf{x}_j)$ is a vector with N components, given by the integrals

$$G^n_{\ i}(\mathbf{x}_j) = \int_{R_n} g_i(\mathbf{x}_j, \zeta) dV. \qquad (4)$$

The index i runs from 1 to 3 and j varies over the observation points, from 1 to M. One may compute the coefficients $G^n_i(\mathbf{x}_j)$ using either an analytical or semi-analytical Green's function, or numerically, using finite differences or finite volume techniques.

In our application to InSAR data we will need to modify expression (3), which provides the displacements along each coordinate axis. InSAR range change, r, is a projection of the displacement vector onto the look vector $\mathbf{l}$ pointing in the direction of the satellite (Ferretti 2014):

$$r(\mathbf{x}_j, t) = \mathbf{l} \cdot \mathbf{u} = l_i u_i(\mathbf{x}_j, t). \tag{5}$$

Substituting the representation of $u_i(\mathbf{x}_j, t)$ given in eq. (3) produces

$$r(\mathbf{x}_j, t) = \mathbf{m}_j \cdot \mathbf{v}, \tag{6}$$

where

$$\mathbf{m}_j = l_i \mathbf{G}_i(\mathbf{x}_j), \tag{7}$$

and the dependence of $\mathbf{v}$ upon t is implicit. Given a large collection of data from various observation points $\mathbf{x}_j$, we can write eq. (6) compactly as a matrix-vector equation

$$\mathbf{r} = \mathbf{M} \cdot \mathbf{v}, \tag{8}$$

where $\mathbf{M}$ is a matrix whose columns signify the grid blocks of the model and whose rows signify the particular observation point and the components of $\mathbf{r}$ correspond to different measurement points $\mathbf{x}_j$ as j varies over the number of observations.

2.1.2 The inverse problem

Eq. (8) relates volume changes in the grid blocks of the model $\mathbf{v}$ to range changes at the observation points $\mathbf{r}$, encapsulating the forward problem. In the inverse problem one attempts to solve, or invert, eq. (8) for estimates of the volume changes $\mathbf{v}$. Due to errors in the observations and the averaging or smoothing effects of the forward operator, it is not advisable to solve for $\mathbf{v}$ directly. The most common approach to deal with errors in the observations is to minimize the sum of the squares of the residuals, written here as

$$\Sigma^2 = (\mathbf{r} - \mathbf{M} \cdot \mathbf{v})^t \cdot (\mathbf{r} - \mathbf{M} \cdot \mathbf{v}). \tag{9}$$

Minimizing this quantity will produce volume change estimates that fit most of the data, and the method works well for normally distributed errors (Menke 1989). If there are significant variations in the errors associated with the observations, it will be necessary to weight each data constraint by its standard error.

An additional issue is the averaging or smoothing effect of the forward operator and the non-uniqueness of the estimated volume changes. Important information may be lost when we record the deformation at the surface of the Earth, leading to non-uniqueness even when we formally have more data than unknowns. In particular, the high spatial frequencies of the displacement field decay with distance away from the source. For a deep source we may only retain the low frequency component of the displacement field at the surface. Uncertain data, variations in the inversion algorithm, and variations in model constraints also contribute to ambiguity or uncertainty in the model estimates, compounding the non-uniqueness. Including a roughness or model norm penalty term to address the non-uniqueness, will tend to produce an overly smoothed or attenuated solution. The loss of resolution will significantly impact the estimated stress changes because they depend upon the spatial gradients of the displacement field.

While we cannot remove the non-uniqueness associated with the inverse problem, we can construct a model that both satisfies the data and is compatible with field operations that are driving the reservoir volume changes and the strain in the overburden. Our approach is to take advantage of the fact that the displacements are generated by measured quantities, the fluid fluxes into and out of each grid block. For example, given a significant net injection into a particular grid block, one might expect a large pressure increase and a larger fractional volume change for that grid block. Therefore, we will include a term that penalizes volume changes deviating from expected values, based upon production and injection into that block, denoted by $\mathbf{v}_p$. In particular, we minimize the sum of the squares of the deviations from the volume changes estimated from the production and injection data,

$$\Pi^2 = (\mathbf{v} - \mathbf{v}_p)^t \cdot (\mathbf{v} - \mathbf{v}_p). \tag{10}$$

The relationship between the net fluid volume change within a grid block and the volume change of that grid block can be complicated by the effects of multiphase flow, thermal expansion and contraction, and material damage. Therefore, the predicted volume changes $\mathbf{v}_p$ can require a sophisticated model and will be subject to some error. In the Appendix we provide an example of a simple model, based upon grid blocks that behave in a poroelastic fashion. Such a model provides a relationship between the injected fluid volumes and the predicted aggregate volume change of the grid block.

The total penalized misfit is given by the weighted sum of the data misfit plus the sum of the squares of the deviations from volume changes predicted from the volume fluxes

$$\Omega^2 = \Sigma^2 + w_p \Pi^2. \tag{11}$$

The scalar w_p is the weight given to the penalty term and it controls the trade-off between fitting the data and honouring the expected volume changes $\mathbf{v}_p$. A necessary condition for the minimum of Ω^2 is the vanishing of the gradient with respect to the elements of the model parameter vector $\mathbf{v}$, leading to the system of equations

$$\nabla_v \Omega^2 = -\mathbf{M}^t \mathbf{r} - w_p \mathbf{v}_p + \left[\mathbf{M}^t \mathbf{M} + w_p \mathbf{I} \right] \mathbf{v} = 0. \tag{12}$$

Solving eq. (12) for the volume changes in each grid block results in a penalized least squares estimate, $\hat{\mathbf{v}}$, that is linearly related to the range change observations:

$$\hat{\mathbf{v}} = \left[\mathbf{M}^t \mathbf{M} + w_p \mathbf{I} \right]^{-1} \left[\mathbf{M}^t \mathbf{r} + w_p \mathbf{v}_p \right]. \tag{13}$$

It is evident that as w_p approaches zero this expression converges to the standard least squares solution minimizing the misfit to the observed range changes. Furthermore, if $\mathbf{v}_p$ is taken to be the zero vector then we have a minimum norm solution (Menke 1989). The minimum norm solution is often used in geophysical inversion in order to reduce artefacts due to noise in the observations by eliminating components in the null-space of the inverse problem (Menke 1989).

2.1.3 Assessment: model parameter covariance and resolution

As we shall see in Section 3, very different models can fit the observations within their expected error bounds. Thus, we are faced with questions concerning the uniqueness of the estimated volume changes as well as model parameter uncertainties. Our inverse problem is characterized by a linear relationship between the observations and the unknown parameters, as is evident in eq. (3). There is a well-developed methodology for assessing solutions of such linear inverse problems (Menke 1989; Parker 1994; Tarantola 2005; Aster *et al.* 2013). As in any exercise in parameter estimation there is the issue of the uncertainty associated with the estimates, typically

given by model parameter variances and covariances (Menke 1989). This aspect has been discussed in numerous publications and books. Therefore, techniques for computing model parameter covariances will not be described in detail here. Rather, we shall merely present the expression for the model parameter covariance matrix, given a data covariance matrix $\mathbf{C}_d$. To simplify the presentation we will consider the case in which $\mathbf{v}_p$ is the zero vector in eq. (13), the minimum norm solution (Menke 1989):

$$\hat{\mathbf{v}} = \mathbf{M}^{\dagger}\mathbf{r}, \tag{14}$$

where $\mathbf{M}^{\dagger}$ is the generalized inverse of $\mathbf{M}$ given by

$$\mathbf{M}^{\dagger} = \left[\mathbf{M}^t\mathbf{M} + w_p\mathbf{I}\right]^{-1}\mathbf{M}^t. \tag{15}$$

From eq. (14) we see that the model parameter estimates are linearly related to the observed data. Such linearity leads to the following relationship between the data covariances and the model parameter covariance matrix $\mathbf{C}_m$

$$\mathbf{C}_m = \mathbf{M}^{\dagger}\mathbf{C}_d\left(\mathbf{M}^{\dagger}\right)^t. \tag{16}$$

In geophysics we are faced with additional challenges due to the fact that our parameters are often continuously varying properties rather than discrete quantities. Rock density and volume change due to pressure changes within a reservoir are but two simple examples of continuously varying quantities. As noted by Backus & Gilbert (1968), we can only reliably estimate the spatial averages of properties, such as grid block values in a discretization of the continuous problem. Even then, our data frequently cannot resolve individual block values independently of the values in adjacent grid blocks. In this context, we are led to the concept of model parameter resolution and the resolution matrix (Menke 1989). The resolution matrix characterizes the averaging inherent in estimates of spatially varying geophysical parameters. Specifically, the resolution matrix relates model parameter estimates to a hypothetical 'true' model that satisfies the relationship (8). To make this concrete, consider the estimates of grid block volume changes, given by eq. (14). If the expression (8) is substituted for $\mathbf{r}$ one has

$$\hat{\mathbf{v}} = \mathbf{M}^{\dagger}\mathbf{M}\mathbf{v}, \tag{17}$$

a relationship between $\mathbf{v}$ and $\hat{\mathbf{v}}$. The resolution matrix $\mathbf{R}$ is defined as

$$\mathbf{R} = \mathbf{M}^{\dagger}\mathbf{M} \tag{18}$$

and it may be interpreted as a matrix describing the averaging inherent in forming the model parameter estimates (Menke 1989). In particular, the entries in a row of the resolution matrix denote averaging coefficients describing how elements of the 'true' model $\mathbf{v}$ are combined to form a model parameter estimate. For this reason, the rows of the resolution matrix are known as averaging kernels. With the full resolution matrix it is possible to construct a measure of spatial resolution (Jackson 1979), the resolving width associated with a particular block.

We have briefly outlined the conventional model assessment for linear problems, covering our particular inverse problem [see eq. (8)]. Note that when the inverse problems becomes sufficiently large, with hundreds of thousands of unknowns, it can be difficult to evaluate the explicit expressions for the standard analysis and approximate methods may be required. This was frequently the case for global tomographic inverse problems for the velocity structure of the whole Earth derived from seismic arrival times (Hager & Clayton 1989; Inoue *et al.* 1990; Pulliam *et al.* 1993). In order to work around the computational difficulties, approximate methods

such as spike and checkerboard tests were developed in order to estimate model parameter resolution (Humphreys & Clayton 1988; Hager & Clayton 1989; Inoue *et al.* 1990; Pulliam *et al.* 1993). A spike test estimates a column, rather than a row, of the resolution matrix (Inoue *et al.* 1990). Subsequently, the formal resolution matrix was calculated using a massively parallel computer (Vasco *et al.* 1993). Using an iterative Lanczos algorithm, it proved possible to approximate the resolution covariance matrices for problems involving over 1 million data constraints and hundreds of thousands of unknowns (Vasco *et al.* 1999; Vasco & Johnson 2003). In spite of these advancements, checkerboard tests are still used to approximate model parameter resolution (Wang *et al.* 2015) for linear inverse problems of moderate size, perhaps for their ease of implementation. The drawback to such approximations are that the spike tests only approximate one column of the resolution matrix and checkerboard resolution estimates depend upon the spatial length scale of the checkerboard pattern. In this work we shall estimate the resolution and covariance matrix elements directly, using the methods of Vasco *et al.* (1999) and Vasco & Johnson (2003). Then we can display the diagonal elements of the resolution matrix, as well as particular rows of the resolution matrix. A row of the resolution matrix, an averaging kernel, displays the degree of averaging that is inherent in a particular model parameter estimate.

2.2 Calculating the displacement in the overburden

The displacement in the overburden follows from eq. (3). If we substitute the volume change estimate (13) into eq. (3) and rewrite it to highlight the fact that the expression is valid for all points in the medium outside of the source region, we have an estimate of the displacement

$$\hat{u}_i(\mathbf{x}, t) = \mathbf{G}_i(\mathbf{x}) \cdot \hat{\mathbf{v}}(t). \tag{19}$$

Note that the dependence on spatial location $\mathbf{x}$ is contained in the Green's function and not in the volume changes $\mathbf{v}$. The estimated displacements are linearly related to the volume changes, and correspondingly linearly related to the observed range changes.

2.3 Estimating the stress change

Assuming that the region around the reservoir behaves elastically during the time interval of interest, the stress change during that period is given by

$$\Delta\hat{\sigma}_{ij} = \mu\left(\frac{\partial\hat{u}_i}{\partial x_j} + \frac{\partial\hat{u}_j}{\partial x_i}\right) + \lambda\frac{\partial\hat{u}_k}{\partial x_k}\delta_{ij}, \tag{20}$$

(Kennett 1983), where $\mu(\mathbf{x})$ and $\lambda(\mathbf{x})$ are the shear modulus and Lame parameter for the overburden. Using eq. (3), the expression for a spatial derivative of the estimated displacement may be written as

$$\frac{\partial\hat{u}_i}{\partial x_j} = \frac{\partial\mathbf{G}_i}{\partial x_j} \cdot \hat{\mathbf{v}}(t). \tag{21}$$

Substituting for all the derivatives in eq. (20) produces a relationship between the volume change estimates and the change in stress

$$\Delta\hat{\sigma}_{ij} = \left[\mu\left(\frac{\partial\mathbf{G}_i}{\partial x_j} + \frac{\partial\mathbf{G}_j}{\partial x_i}\right) + \lambda\frac{\partial\mathbf{G}_k}{\partial x_k}\delta_{ij}\right] \cdot \hat{\mathbf{v}}. \tag{22}$$

Because of the spatial derivatives, the quantity in square brackets is a roughening operator acting upon the estimated volume changes.

For sufficiently large stresses and strains, the overburden may behave in a nonlinear fashion, either as a nonlinear elastic material

or inelastically. For a nonlinear elastic material the elastic moduli depend upon the stress or strain. For the roughly one-month intervals considered in the application below, we shall assume incremental linear elastic behaviour. However, for long time intervals it may be necessary to account for the variations of μ and λ with stress or strain. With the exception of the scaling estimates in the Appendix, we make no assumptions about the behaviour of the source region within the reservoir, as it is a singular region and diatomite may behave as a nonlinear plastic material (Bruno & Bovberg 1992).

3 APPLICATION

We illustrate the methodology with an application to observations of surface deformation gathered over an oil field in the San Joaquin Valley of California.

3.1 Geological setting

The field is part of the Tulare fold belt, a series of northwest trending asymmetric anticlines and synclines in the Plio-Pleistocene Tulare formation (Farley 1990). It is one of a series of fields, including Belridge, Cymric, Lost Hills, Buena Vista, Elk Hills, Midway Sunset, Railroad Gap, McKittrick, and Asphalto, that produce from diatomite reservoirs. Diatomite is a high porosity (45–70 per cent) rock, consisting of the shells and fragments of diatoms mixed with varying amounts of clay and sand (Fredrich *et al.* 2000). The depositional environment is thought to have been a deep-marine fan system extending into a basin bounded by the Sierran block to the east and the Salinian block and Gabilan range to the west (Miller & McPherson 1992). Given its high porosity, diatomite can be extremely compressible and, as discussed below, reservoir production and injection have led to significant surface deformation. Furthermore, diatomite is a low permeability rock (0.1 to several millidarcies) saturated by very viscous oil, requiring cyclic steaming in order to recover a significant fraction of the oil (Kumar & Beatty 1995). The diatomite reservoir is overlain by a sedimentary sequence of sands, shales, and pebble conglomerates of the San Joaquin and Etchegoin formations. The top of the diatomite is now generally between 200 and 300 m below the ground surface. The primary structural feature is an anticline with a gradually dipping limb to the west, containing most of the field, and a steeply dipping limb to the east of the field (Fig. 1). Stress measurements (Mount & Suppe 1987) suggest that the anticline appears to be growing along an axis subparallel to the San Andreas fault, caused by compression oriented perpendicular to the fault.

3.2 Material properties

The wide-spread compaction, and associated surface deformation and well failures, in diatomite reservoirs (Myer *et al.* 1996; Fredrich *et al.* 2000), has motivated several studies of the mechanical behaviour of these rocks and of the material in the overburden (Stosur & David 1976; Strickland 1985; Bruno & Bovberg 1992; Fossum & Fredrich 1998; Fossum & Fredrich 2000; Fredrich *et al.* 2000). Unfortunately, little published core data is available for the overburden formations. For the San Joaquin Formation, Fossum & Fredrich (2000) refer to the study of five core samples from the Lost Hills field by Bruno & Bovberg (1992). In those studies a Mohr-Coulomb failure envelope was defined and the cohesion and angle of internal friction were estimated. In addition, Bruno & Bovberg (1992) found that the average Young's modulus for the samples lies between 0.3 and 1.0 GPa, and determined that the mean Poisson's ratio was 0.25.
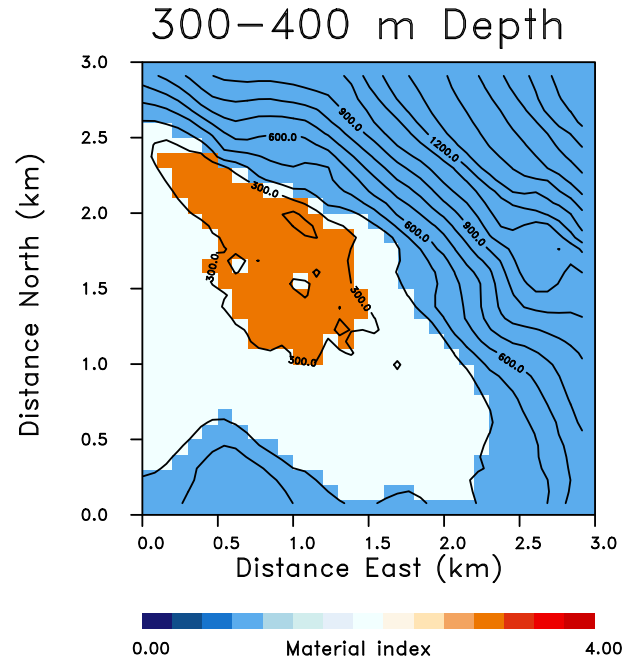

Figure 1. Variation in the depth to the top of the diatomite, as indicated by the contour lines, in the central California reservoir. The colours indicate the spatial variation of the distribution of the four materials defining the reservoir volume in the depth interval of 300–400 m. Dark blue signifies the near-surface sediments, light blue indicates the Tulare formation, orange denotes the diatomite (Opal A) and red represents the lower diatomite (Opal C). The lower diatomite is not present in this depth section.

Fredrich *et al.* (1996) fit a Drucker–Prager failure model to the alluvium and samples from the Upper and Lower Tulare formations. Much more information is available in the literature on the properties of the diatomite itself, both the reservoir material (Opal A) and the porcelanite (Opal CT) that underlies the reservoir (Stosur & David 1976; Strickland 1985; Fossum & Fredrich 1998; Dietrich & Scott 2007).

There are several unpublished sonic logs and density logs through the overburden and the diatomite. The sonic logs recorded both compressional and shear propagation times that may be used to calculate seismic velocities. The properties for specific formations are consistent for the well logs that we examined. Therefore, these well logs can be used to estimate dynamic elastic moduli for the major layers in the overburden. The dynamic moduli are converted to static moduli by scaling Youngs modulus by 0.22 and then transforming to Lames parameter $\lambda(z)$ and the shear modulus $\mu(z)$ (Fig. 2). The values of the corresponding Bulk moduli for this model are of the same order as those cited in the constitutive model of Fossum & Fredrich (2000), varying from under 0.15 GPa to over 0.30 GPa for depths between the surface and 500 m. The depths of boundaries do vary across the field due to the anticlinal structure and corresponding deviations in the thickness of the formations. The depths of the boundaries shown in Fig. 2 correspond to those found in a well intersecting the west central portion of the field. However, the western limb of the anticlinal structure is gentle and the layer boundaries do not vary significantly over most of the field (Fig. 1).

3.3 Monitoring deformation using Synthetic Aperture Radar

Because the fields in the San Joaquin Valley are characterized by soft and porous formations that are quite thick and rather
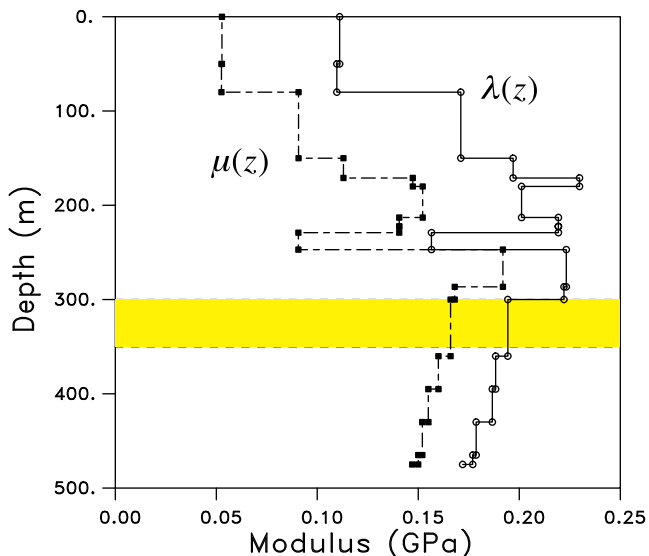
Figure 2. Depth variation of the Lame parameter ($\lambda(z)$) and the shear modulus ($\mu(z)$) within the overburden and the diatomite. The reservoir interval in the model is indicated by the yellow area between the two dashed lines.

shallow, oil production has generated observable subsidence at the ground surface (Bowersox & Shore 1990; Bruno & Bovberg 1992; De Rouffignac & Bondor 1995). Such subsidence has been actively monitored in several fields. For example, starting in 1989; Global Positioning Satellite (GPS) surveys have been conducted in the Lost Hills Field over an array of some 70 monuments (Bruno & Bovberg 1992). In 1998 it was shown that Synthetic Aperture Radar (SAR) could provide high-resolution images of the deformation due to oil production in the San Joaquin Valley (Fielding *et al.* 1998).

Following the successful demonstration by Fielding *et al.* (1998), SAR data have been used to monitor deformation above several oil fields in central California. A total of 156 images were acquired between 2000 September 10 and 2013 February 10 and processed to extract stable scatterers and their associated range change (Ferretti *et al.* 2001, 2011). The semi-arid, sparsely vegetated ground surface and the abundance of man-made structures provided excellent conditions for SAR monitoring, resulting in over 1800 imaging points per square kilometre. The precision of the deformation rate is roughly 1 mm yr^{-1} while the error associated with the range change is less than 5 mm. An example of the estimated range change is shown in Fig. 3 for a subset of the field. The time-series for the scatterers were reinterpolated onto monthly range changes, in this case for February 2001. The surface deformation associated with the injection and production of fluids from a large number of wells comprising the field is evident in Fig. 3.

3.4 Estimating reservoir volume changes

The first step in the estimation of stress changes involves the determination of volume changes in the reservoir from the observed InSAR range changes, such as those shown in Fig. 3. The estimates of volume change are subject to constraints provided by the net fluid volume fluxes due to injection and production. These constraints, in the form of the penalty term given in eq. (10), are derived from the reservoir production and injection data. The reservoir interval extends from 300 to 400 m in depth, just below the top of the diatomite. The reservoir volume is subdivided into a 30 × 30 grid of cells, 100 m on a side. The field operator provided monthly mea-
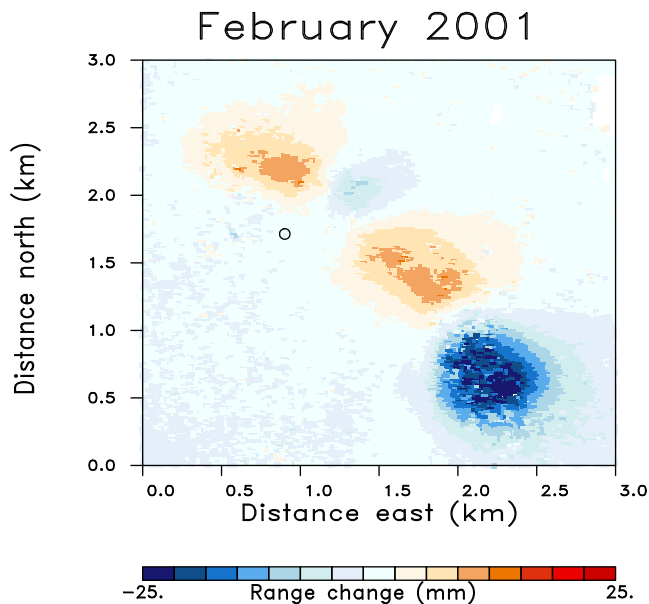

Figure 3. Range change obtained from RadarSat Interferometric Synthetic Radar (InSAR) data. Positive range change indicates increasing distance to a reference point in space, typically signifying subsidence. The open circle identifies the well in which a multifinger caliper log was run.
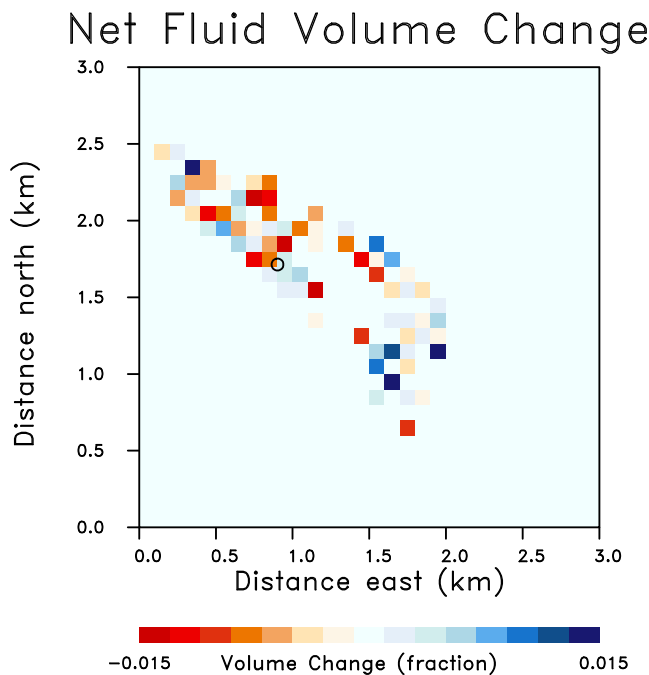
Figure 4. Net fluid volume change during the month of February 2001, in terms of the volume fraction of the grid block. The grid blocks are 100 m (east–west) by 100 m (north–south). The open circle identifies the well in which a multifinger caliper log was run.

surements of injected and produced fluids [steam, water, oil, and gas] from the wells in the field. The fluid volumes of steam, water, oil, and gas at reservoir conditions, from wells intersecting each grid block, are added up to calculate the net fluid volume change. An example of the net fluid volume change for February 2001, in terms of the volume fraction of the reservoir grid block, is plotted in Fig. 4.
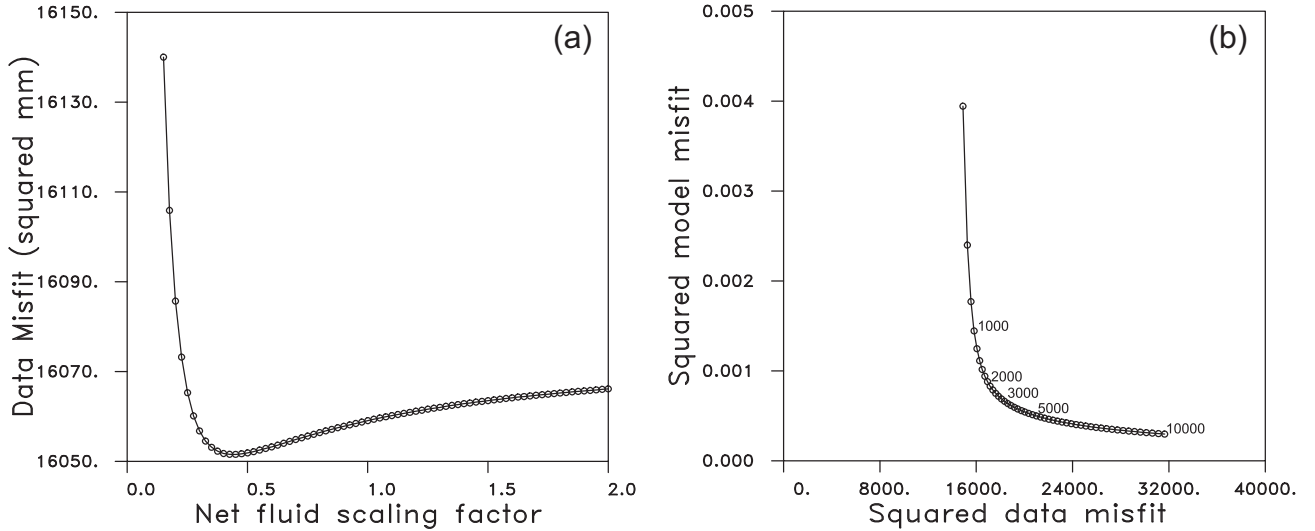
Figure 5. (a) Total misfit for 81 inversions conducted for varying values of the coefficient relating grid block volume change to fluid volume change. (b) Curve displaying the trade-off between the squared data misfit and the squared model misfit, parameterized by the weighting factor w_p. The value of w_p at specific points is indicated by the numerical labels. As is evident from the curve, as w_p increases the model misfit decreases while the data misfit increases.

Because the fluid volume introduced into a porous medium does not lead to an equivalent volume change in the medium itself, a scaling factor was required. The scaling factor relates fluid volume change to grid block volume change. In the Appendix we discuss the considerations that enter into the calculation of the scaling factor when the grid block behaves poroelastically. The discussion in the Appendix is for primarily for illustration, we use an empirical approach to actually estimate the scaling factor. Specifically, we conducted a series of constrained inversions and examined the variation in data misfit as a function the value of the scaling factor (Fig. 5a). A factor between 0.35 and 0.45 appears to produce the best fit when the fluid volume constraints are included. Once a value of 0.25 is exceeded, the total misfit does not seem to be a strong function of the scaling. The variations in Fig. 5(a) are notable because the scale has been expanded significantly in order to highlight the small changes. The value of the scaling factor lies between 0.1 and 1, the range estimated in the Appendix. A factor of 0.35-0.45 corresponds to an average grid block porosity between 12 per cent and 14 per cent.

Both the estimates of volume and stress changes depend upon the nature of the Green's functions $g_i(\mathbf{x}, \boldsymbol{\zeta})$ [see eq. (2)]. Because the western limb of the anticline defining the reservoir has a very shallow dip, as indicated in Fig. 1, we will used a layered elastic model to represent the overburden above the field (Fig. 2). Accordingly, our Green's functions will be calculated using a propagator technique developed by Wang *et al.* (2003, 2006) for a layered elastic or viscoelastic medium. The next level of complexity is to include the depth variations of the boundaries, as shown for the top of the diatomite reservoir in Fig. 1. We have also computed Green's functions for a model containing variable boundaries and four materials (Fig. 1), using a finite difference algorithm. We found that the estimated volume changes were not significantly different when we used the finite difference approach. Therefore, we will adopt the layered Green's functions computed using the method of Wang *et al.* (2006). As a check, we will compare the stress estimates to one based upon a full 3-D model, as shown in Fig. 1, computed using a finite-difference computer code.

The solution that minimizes the penalized least squares objective function was found by solving the necessary conditions for

a minimum, eq. (12). The iterative sparse solver LSQR (Paige & Saunders 1982) was used to solve the system of eqs (12). For comparison, a conjugate gradient solver (Press *et al.* 2007) and the explicit numerical evaluation of expression (13) were used to minimize the penalized misfit Ω^2 [see eq. (11)] and found to produce the same essential result. A trade-off curve was constructed by conducting 51 inversions where the weighting parameter w_p was varied between 0 and 10 000 in a systematic fashion. The curve displaying the squared data misfit against squared model misfit for each value of w_p is plotted in Fig. 5(b). From this curve it appears that inversions where w_p lies between 1000 and 5000 produce reasonable fits to both the observed range changes and the prior total fluid volume changes $\mathbf{v}_p$. For the results that follow, we set w_p equal to 1111 in order to provide a reasonably good fit to the range change data.

Considering the data and constraints for February 2001 we estimated both a minimum norm solution ($\mathbf{v}_p = 0$) and a solution constrained by the injection and production measurements (Fig. 6). There is fairly good agreement between the reservoir net volume change (Fig. 4) and the constrained solution (lower panel, Fig. 6b). The minimum norm solution (upper panel, Fig. 6a) is smoother, evidence of the loss of resolution with depth associated with this inverse problem. The constrained inversion displays characteristics of both the net fluid volume change in Fig. 4 and the minimum norm inversion (Fig. 6a). In Fig. 7, we plot the difference between the constrained inversion in Fig. 6(b) and the net fluid volume change in Fig. 4. The differences are as large as 50 per cent of the peak variations in the constrained inversion and show a pattern very similar to anomalies in the minimum norm solution (Fig. 6a). Thus, the constrained inversion does not simply replicate the prior net fluid volume model. Rather, the inversion result strikes a balance between fitting the observations and honouring the prior information.
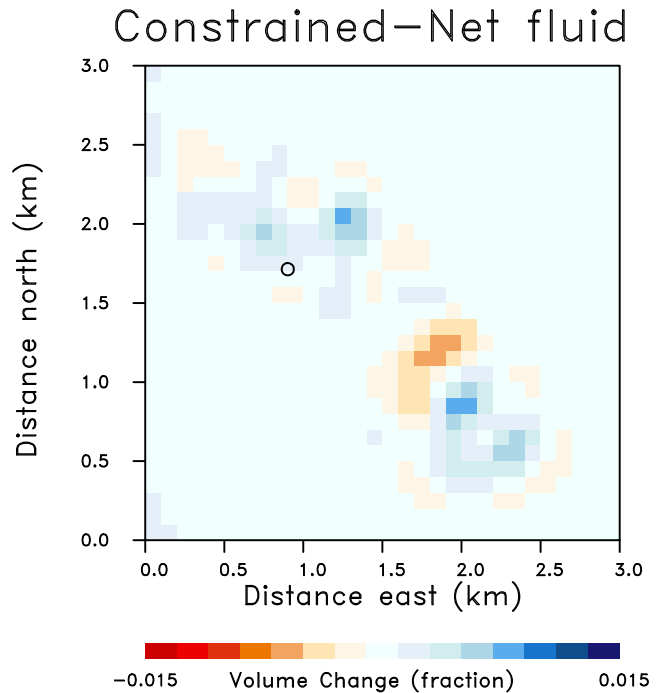
The predicted range changes, calculated using both the constrained and minimum norm solutions, are shown in a map view in Fig. 8, and in Fig. 9 as the calculated range change plotted against the observed range change. In both figures one observes that the constrained solution fits the data about as well as the minimum norm solution, with correlation coefficients of 0.9778 and 0.9779, respectively. The change in variance for the inversion with a minimum norm prior was from 381 494.5 to 15 956.3, a 95.82 per cent
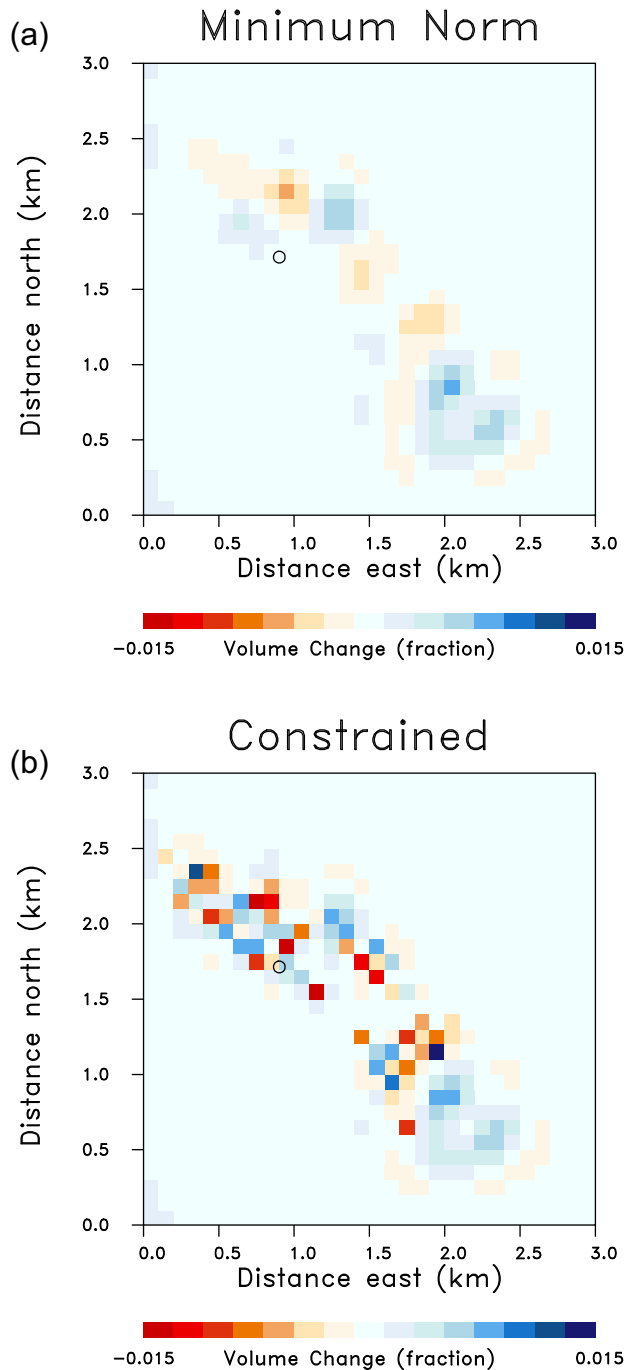
Figure 6. (a) Fractional volume change obtained from an minimum norm inversion of the range change data in Fig. 3. (b) Distribution of fractional volume changes from a constrained inversion of range change observations. A penalty term was included in the inversion biasing the solution to honour the net volume change due to fluid injection and production in each grid block, shown in Fig. 4.


Figure 7. Difference between the results of an inversion of range change data for reservoir volume change that is constrained by reservoir net injected and produced fluid (Fig. 6b) and the net fluid volumes used to constrain the model (Fig. 4).

variance reduction. The variance for a model constrained by the net fluid flux due to injection and production was reduced to 16 044.7, a variance reduction of 95.79 per cent. Thus, it appears that the reservoir fluid volume flux constraints do not degrade the fit to the observations significantly. In the top panel of Fig. 9 we have plotted the range change calculated using the net fluid volume change model (Fig. 4). Observe that the net fluid volume model does not fit the range change data, indicating that the inversion must make

significant changes in the model in order to agree with the measured values. In Fig. 10, the root mean squared (RMS) misfit is plotted for monthly intervals from 2001 until 2010. The RMS misfit is essentially identical for both the minimum norm and constrained inversion over the entire time interval.

The fact that two different models produce equivalent fits to the observations reveals the non-uniqueness inherent in the inversion of InSAR range change observations for volume changes at depth. In an effort to quantify the non-uniqueness we calculate the resolution matrix **R**, defined by eq. (18). The approach, described in Vasco *et al.* (1999, 2002a) and based upon the singular value decomposition (Noble & Daniel 1977), is used to construct the entire resolution matrix. The diagonal elements of the resolution matrix, plotted in Fig. 11(a), provide a quick estimate of one's ability to recover the volume change associated with an individual block, independently of the values in other blocks. Eqs (17) and (18) indicate that as the resolution improves and we can resolve individual block values, the resolution matrix approaches an identity matrix with ones on the diagonals and zeros elsewhere. Thus, for a well resolved model the diagonal elements of the resolution matrix approach unity and the averaging kernels approach impulse functions. The diagonal elements of the resolution matrix (Fig. 11a) indicate that the best resolution is found for blocks at the corners of the model, with values near 0.5, while the resolution at the edges of the model is around 0.3. For grid blocks in the interior of the model the diagonal elements of the resolution matrix are around 0.2. We gain more insight by examining the averaging kernels associated with four grid blocks (Fig. 12). For locations in the interior of the model the estimated volume change is an average over all of the surrounding cells, with significant averaging over a diameter of 300 m. Furthermore, there are oscillations in the averaging coefficients indicating trade-offs between positive and negative volume changes. For grid blocks at the edges and corners of the model the averaging is truncated by
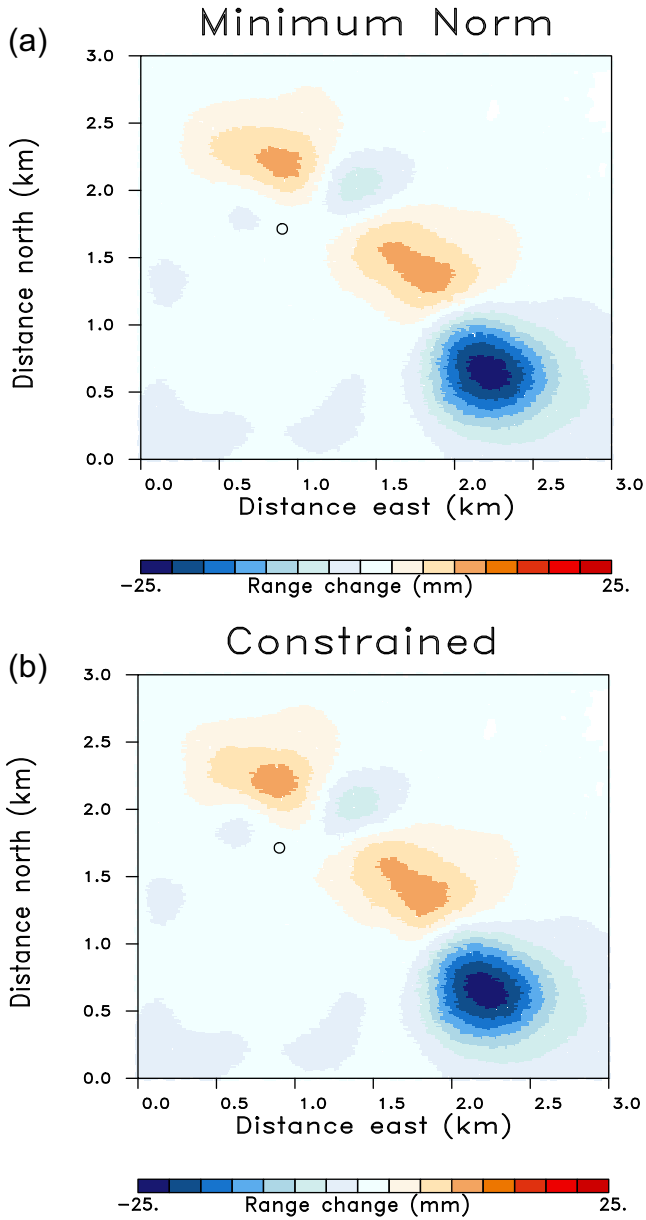
Figure 8. Predicted range change based upon (a) the minimum norm model and (b) a constrained model biased to fit the fluid volume fluxes for each grid block.

the boundary of the model, resulting in less averaging and trade-off, and higher model parameter resolution. Hence, without a penalty term biasing the solution to a rougher model, the minimum norm solution will incorporate the smoothing indicated by the averaging kernels in Fig. 12.

In addition to the model parameter resolution, there is the issue of model parameter uncertainty to contend with. That is, due to errors in the observations there will be errors in the estimated model parameter, given by eq. (13). The resulting model parameter covariances are given by expression (16), where $\mathbf{C}_d$ are the data covariances, and $\mathbf{M}^\dagger$ is the generalized inverse (15). The data covariance matrix can be complicated, with off-diagonal terms arising from spatially correlated data errors due to atmospheric effects (Hanssen 2001). Because we do not have any information on the spatial correlation of the data errors we will assume that the covariance matrix is diagonal. From the InSAR data reduction, we have
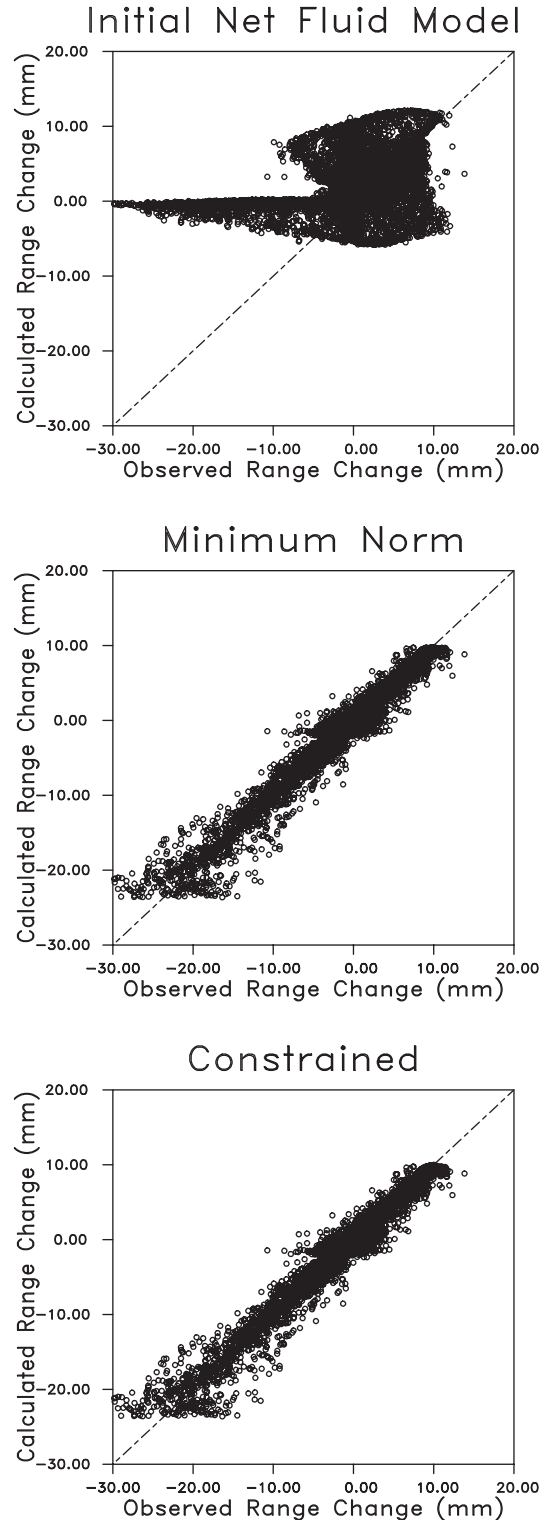
Figure 9. A plot of calculated range change plotted against the observed range change. (a) The calculated range change is based upon the net fluid volumes plotted in Fig. 4. (b) The range changes were from a minimum norm model that minimizes a linear combination of the misfit to the observations and the model norm. (c) The range changes are based upon a model that minimizes the misfit to the data and minimizes the deviations from the injected and produced fluid volumes in each grid block.
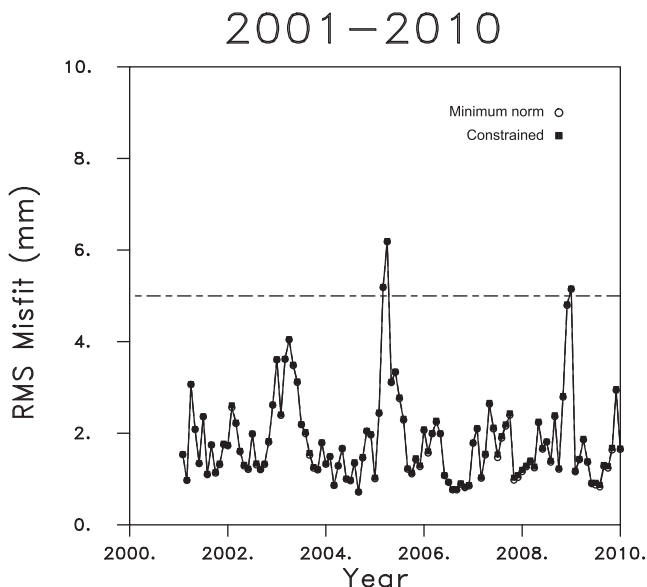
Figure 10. The root mean squared (RMS) data misfit, computed on a monthly basis, for InSAR monitoring from 2001 to 2010. Misfit for both the minimum norm solutions and for solutions constrained by reservoir production and injection data are shown by the open circles and filled squares, respectively.

estimates of the standard error of each datum and these vary as a function of distance from the reference point used in the analysis (Ferretti 2014). In general, the average data error is of the order of 5 mm. The resulting model parameter standard errors, derived from the variances of the covariance matrix (16), are plotted in Fig. 11(b). The model parameter errors are of the order of 0.002, roughly 13 per cent of the peak variation of the fractional volume (0.015). Note that there is a trade-off between the model parameter resolution and the model parameter uncertainty. That is, as one tries

to improve the resolution, there will generally be an increase in the model parameter uncertainty (Aki & Richards 1980; Menke 1989; Aster *et al.* 2013).

### 3.5 Calculating the stress change

The stress changes are found from the volume change estimates given by eq. (13). We first calculate the displacements throughout the overburden, then we estimate the stress changes using expression (20). Eq. (22) encapsulates the entire process as a single equation or linear operator applied to the estimated volume changes $\hat{\mathbf{v}}$. The operator depends upon the elastic model of the overburden and the reservoir, the layered structure given in Fig. 2. We plot both the minimum norm estimates of stress change, as well as the constrained estimates for a depth of 180 m (Fig. 13). While the large scale variations are similar, there are significant small-scale differences in the two estimates of stress changes. Such differences might be expected, given the much smoother minimum norm volume change estimates and the nature of the linear operator in eq. (22). It is interesting that, although the patterns vary, the magnitudes of the two sets of changes are comparable for this one month interval. In Fig. 13, we are plotting

$$\sigma_h = \sqrt{\sigma_{xz}^2 + \sigma_{yz}^2},$$

which we will refer to as the horizontal stress or the horizontal traction vector. This quantity is the resolved shearing stress acting across a horizontal plane. It is akin to the stress applied to shear a deck of cards. Such a stress is often responsible for shear failure across a layer boundary and well buckling due to a localization of shear strain. In Fig. 14, we plot the changes in all six components of the stress tensor for February 2001 and for a depth of 180 m. The complicated pattern reflects the rapid spatial variations in volume change that are present in the constrained volume change model (Fig. 6b).
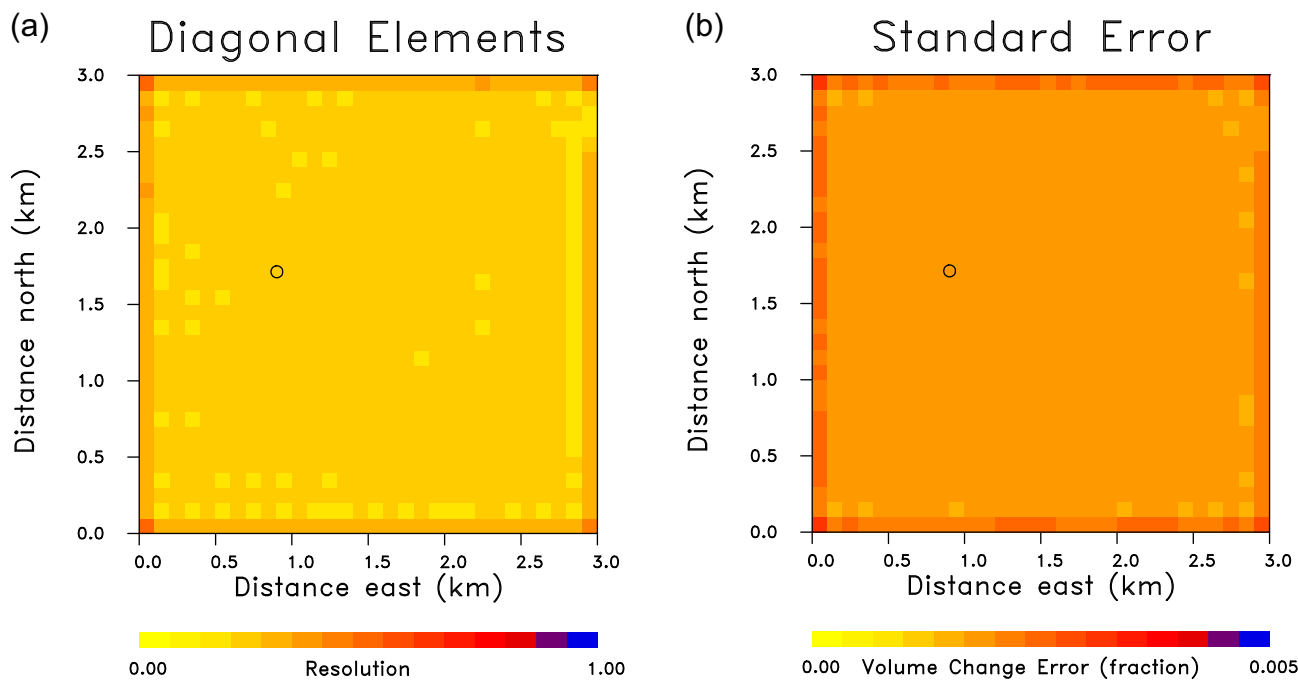

Figure 11. (a) The diagonal elements of the resolution matrix, plotted in the locations of their respective grid blocks. (b) The square root of the diagonal elements of the covariance matrix, producing estimates of the model parameter standard errors, plotted as the volume change fraction.
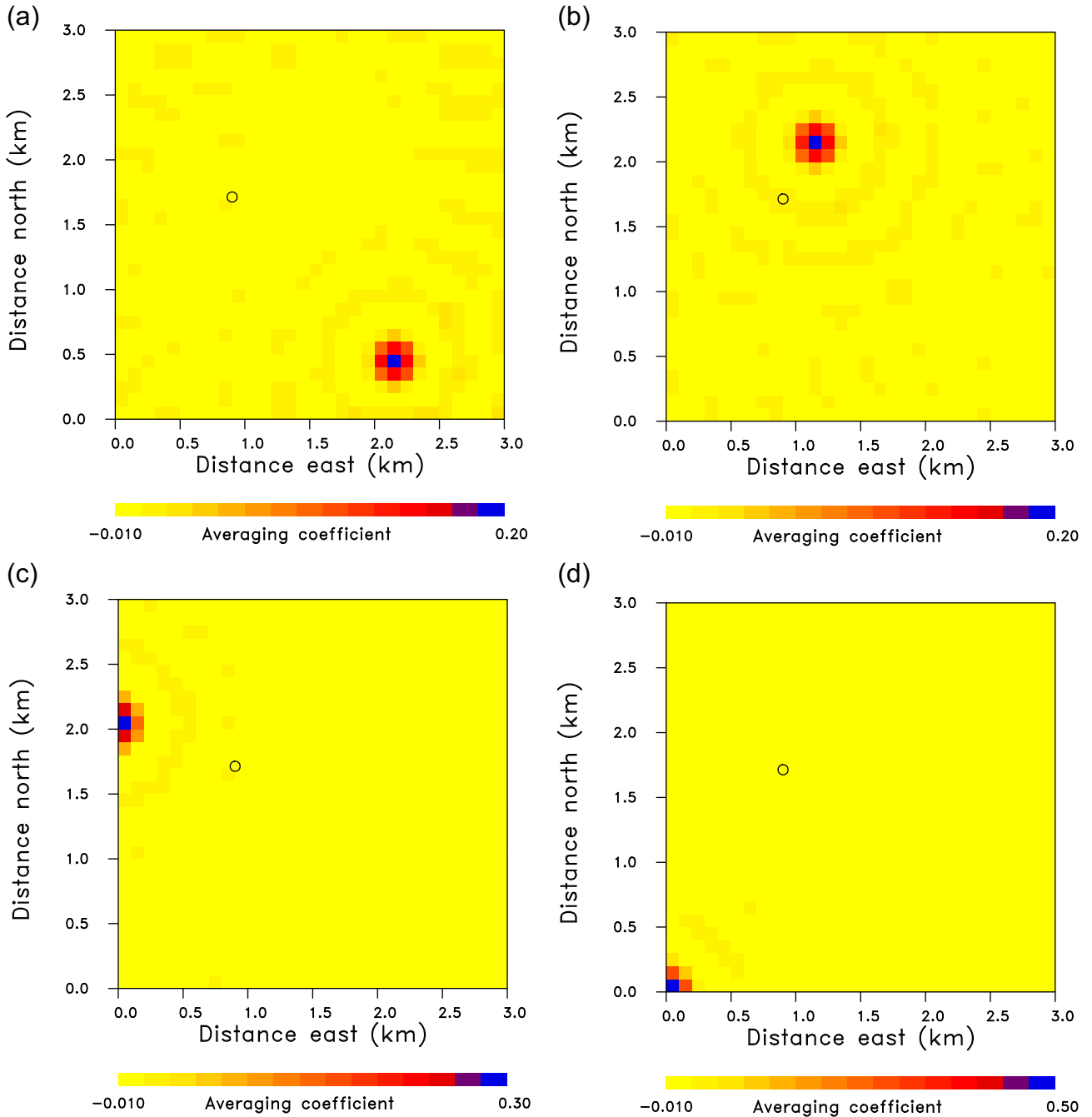
Figure 12. Four averaging kernels corresponding to two interior grid blocks, a grid block at the edge of the model, and a grid block in a corner of the model.

Both the inverse problem for reservoir volume change, and the forward problem of calculating stress change depend upon the elastic coefficients. Therefore, the estimated stress changes depend in a nonlinear fashion upon the elastic coefficients representing the structure. In general, the estimated stress changes will vary significantly if the elastic properties of the overburden are changed. Therefore, stress estimates based upon the layered Green's function described earlier may contain significant errors due to the topographic variations that are evident in the field (Fig. 1). However, the topographic variations underlying the active areas of the field are rather subdued, and a layered model may well yield sufficiently accurate stress estimates. In an effort to check this, we constructed estimates using different elastic models. First, we calculated the volume changes and resulting stress changes using an elastic model consisting of a uniform layer, representing the overburden, over the diatomite reservoir, represented by a half-space. The bulk modulus of the overburden was 0.23 GPa, an average of the layer values, while the average for the diatomite was 0.30 GPa. The average shear moduli for the overburden and diatomite were 0.09 and 0.17 GPa, respectively. Second, we considered a model with the anticlinal topography shown in Fig. 1. The estimated stress changes, based upon these models, are shown in Fig. 15. The spatial pattern of the stress changes are roughly similar for both models, though they vary in detail and the magnitudes do vary significantly. The agreement seems to be the best in the northwestern portion of the reservoir model, in the area of the crest of the anticline where the topography is flatter.
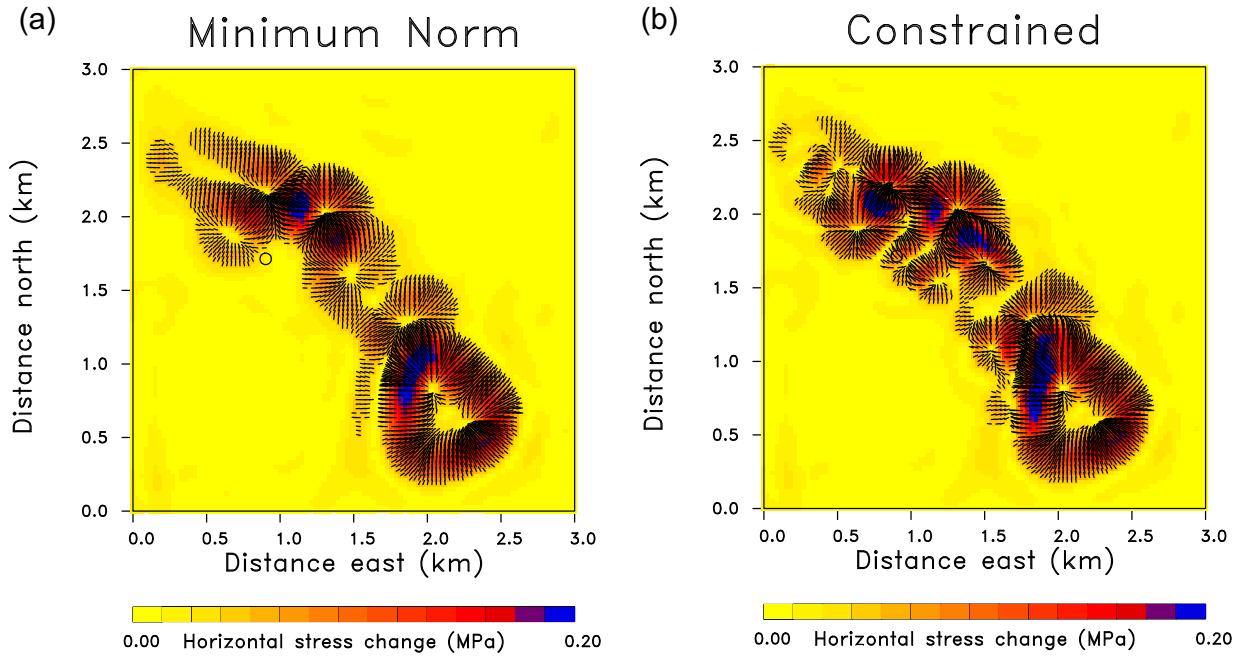
Figure 13. Estimates of horizontal stress changes during February 2001 based upon volume changes estimates using an minimum norm (a) and constrained (b) inversion. The colour scale indicates the magnitude of the horizontal shear stress while the short line segments indicate the orientation.
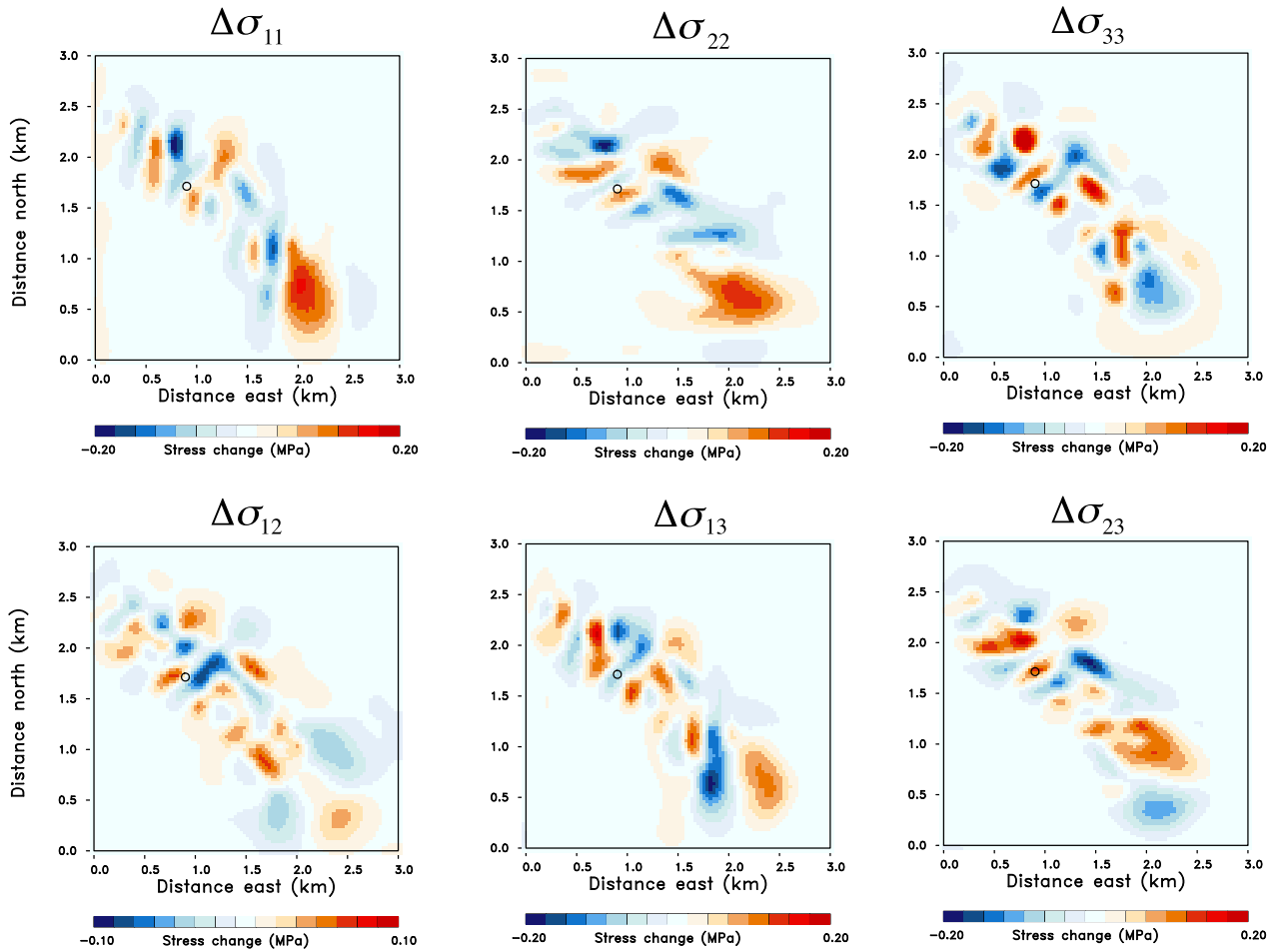
Figure 14. All components of stress change during the month of February in 2001, obtained by an inversion of range change, constrained by the injection and production fluid volumes.
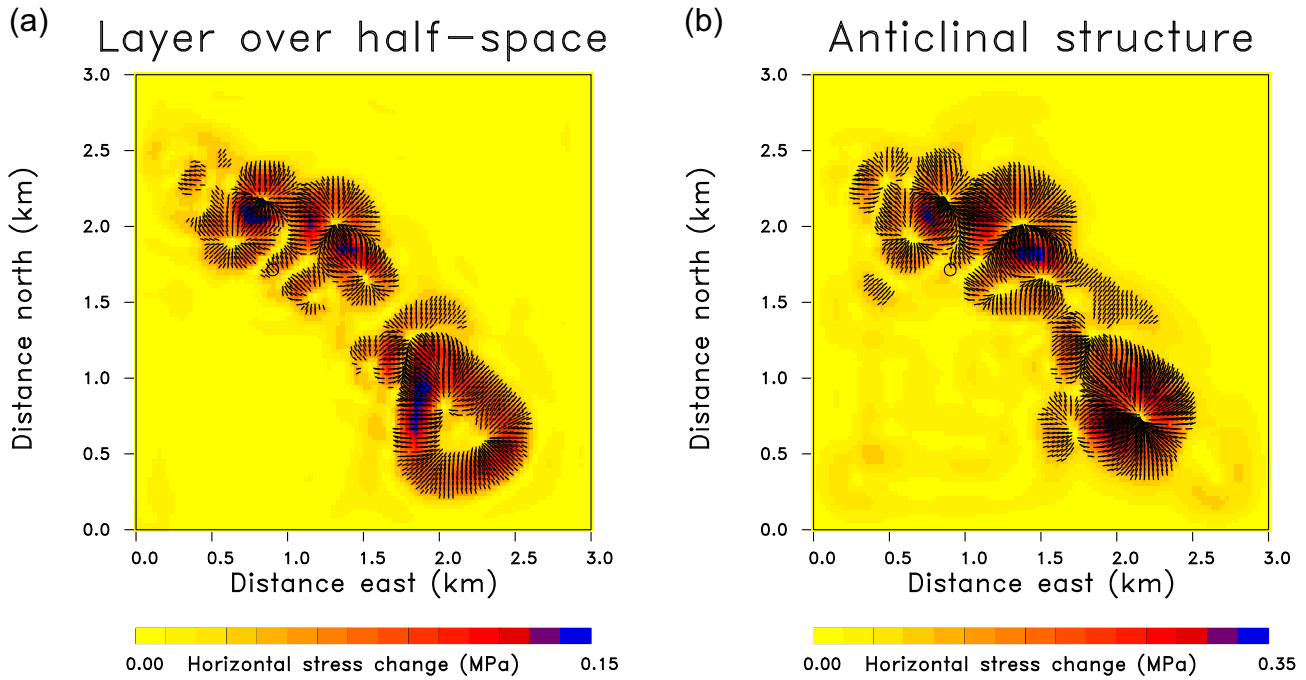
Figure 15. Estimated changes in the horizontal traction vector, obtained using a constrained inversion. Two different elastic models were used in these inversions: (a) a layer over a half-space, and (b) the model shown in Fig. 1, containing an anticlinal boundary between the overburden and the reservoir.

It appears that the general features of the stress estimates for this particular case, such as the length scale of the spatial variations and the general spatial pattern, are probably reliable. This conclusion only applies to the estimates associated with this field, and it is not true for a general elastic model.

The contracted company TRE-Altamira provided estimates of range change for the years 2001 through 2012 and for the first month of 2013. The magnitude of the range change varies significantly in both space and time, as illustrated in Fig. 16 for four selected time intervals. This is most likely due to the changes in fluid injection and withdrawal that occur in the producing field. Overall, the range varies by several centimetres for any given month. Following the procedure described above, we conducted inversions of the range changes, constrained by fluid volume changes estimated from the field fluid fluxes. For the most part, the observations of range change are fit within a root-mean-squared value of 2 mm. The calculated stress changes, for a depth of 180 m, that follow from the inverted volume changes are shown in Fig. 17. The stress change varies much more rapidly in space than does the range change, indicating the influence of the fluid volume constraints and the smoothing of the displacement field with distance from the source. In looking over the monthly intervals between January 2001 and January 2013, we find that the change in the magnitude of the horizontal traction vector varied between 0.1 and 2.0 MPa. As in Fig. 17, for many monthly intervals the peak changes were around 0.5 MPa. For comparison, the compressive stress due to the weight of the overlying material is roughly 4.5 MPa at this depth.

3.6 A comparison with well deformation and failure

While the patterns of stress change are intriguing, we do not yet have an independent method to verify the magnitude of such changes, particularly at depth. That is, there are no measurements of stress or stress changes, as discussed in the Introduction of this paper. In

an effort to determine if the estimates of the strains and the stress changes provide reasonable predictions of observations in the field, we examined results from two wells. In the first well, a caliper log recorded the zones of intense shearing and the depth at which the well was sufficiently bent that no tool could pass that point. In the second well, the failure time is accurately known, down to the exact day, due to the loss of communication with instruments in the well. We use our estimated stress changes to examine the conditions for failure at the well and compare them to the observed time to failure.

As is evident from eq. (22), the calculated stress changes follow from estimates of displacement in the overburden. The InSAR data constrain the projection of displacement onto the satellite look vector, and our fit to the range changes indicate how well we can match observed deformation at the surface. However, for added confidence, we would like to compare displacements measured at depth with predicted values. One set of observations related to the deformation at depth is provided by multifinger caliper logs that were run in three wells in the field. The caliper logs indicate when the orientation of the well changes. In particular, the tool can delineate bends in a given well due to a concentration in strain. The locations of the well that we shall discuss is plotted as an open circle in Fig. 3. In Fig. 18, we compare our predictions of radial displacement as a function of depth in the well, against the depths of zones of observed shear strain. For the most part, the calculated radial displacements of the well are smoothly varying in depth. There are a handful of zones in which there are steep gradients in calculated radial displacements with depth, due to changes in mechanical properties across layer boundaries in the model. From Fig. 18, we see that these zones correlate with the depths at which bends in the well were detected by the caliper logs. The largest and sharpest offset is associated with a tagged zone (denoted by 't') in the caliper log survey, indicating that the well was impassable at the depth and the survey could not continue beyond that point. The size of the jumps in calculated displacements across the layer boundaries are of the order of 1–4 cm, in the range of 0.5–1.5 inches of
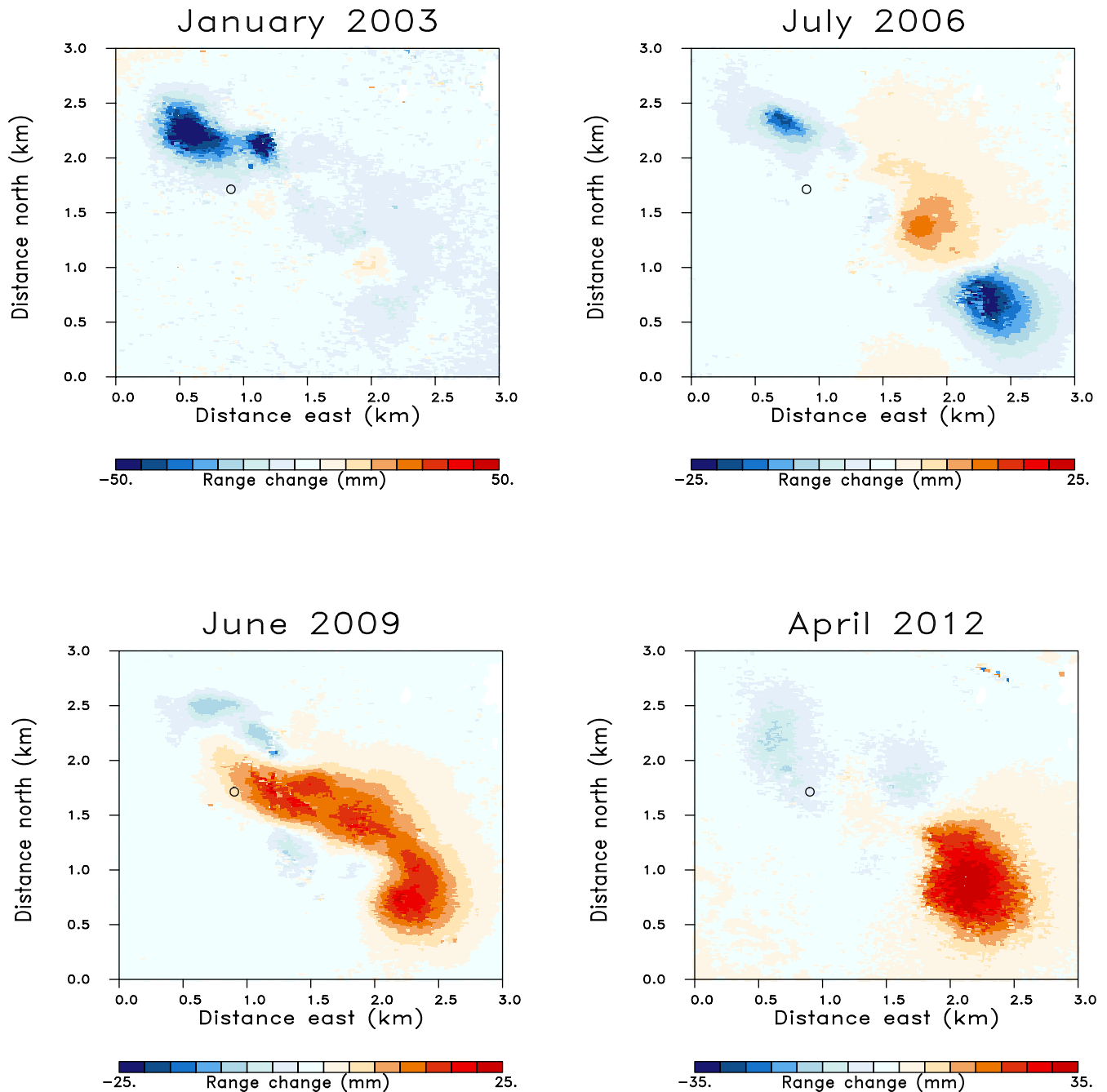
Figure 16. Range changes for four selected one month intervals.

shear offset obtained from the survey. The amount of deformation is sensitive to the geomechanical properties of the medium as well as the level and distribution of deformation induced by the injection and production of fluids in the reservoir. As we approach the depth of the reservoir (300 m) the assumption of elastic behaviour may be called into question because the strains can become quite large and the reservoir may behave plastically. Also, the results are more sensitive to localized variations in the distribution of estimated volume change within the reservoir.

Well failures, due to reservoir deformation, have accompanied oil production from fields in the San Joaquin Valley of California (Bruno & Bovberg 1992; De Rouffignac & Bondor 1995; Myer

et al. 1996; Fredrich *et al.* 2000). For this reason several studies explored the failure characteristics of diatomite, the main reservoir rock (De Rouffignac & Bondor 1995; Fossum & Fredrich 1998; Fredrich *et al.* 2000), and of the overlying sediments where many of the well failures tend to occur (Bruno & Bovberg 1992; Fossum & Fredrich 2000; Fredrich *et al.* 2000). The Drucker-Prager (Drucker & Prager 1952), Cam-Clay (Roscoe *et al.* 1958), and the ESR model (Fossum & Fredrich 2000), an extension of the work of Sandler & Rubin (1979) have been used to model the yield surfaces and shear failure of both the overburden and the reservoir materials.

Given a model of the yield criterion for failure in a given formation we can use our estimated stress changes to determine when
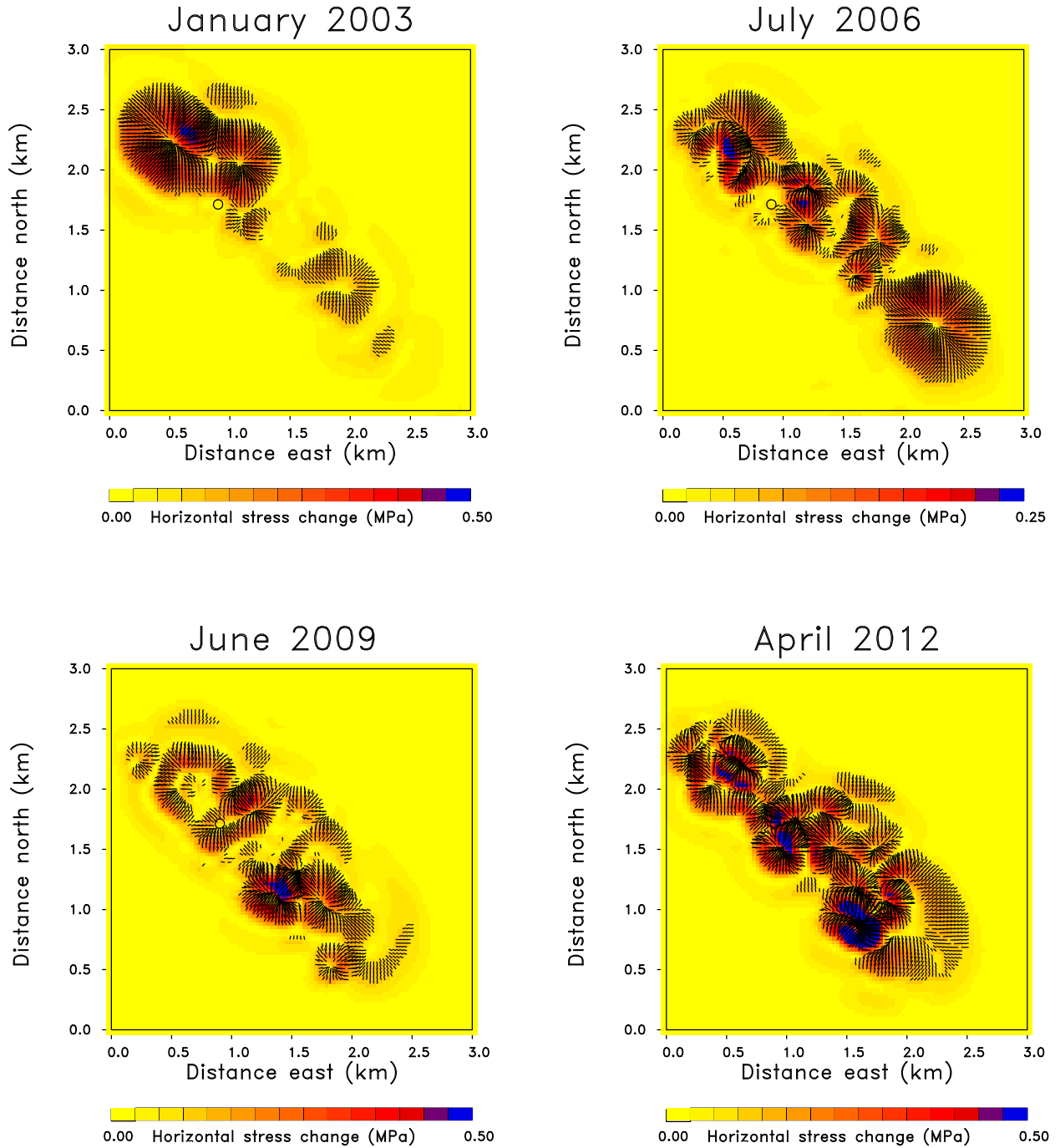
Figure 17. Estimated of horizontal stress changes corresponding to the range change data plotted in Fig. 15. The colour scale indicates the magnitude of the horizontal traction vector, while each line segment indicates the orientation.

failure should occur at a particular location within the overburden. We apply this approach to a well in the field with an accurately documented failure time, located near the western edge of the field. The lifespan for this well is accurately known because its failure resulted in a cessation of data from downhole instrumentation. The well was completed on 2010 August 30 and it failed at a depth of 183 m on 2012 March 31. Two failure criteria were considered, based on properties determined from laboratory experiments discussed in Bruno & Bovberg (1992) and Fossum & Fredrich (2000).

The first failure criterion is a Mohr–Coulomb yield condition, in which the shear strength of a material, or of an interface between

formations, τ_s, depends upon the normal stress on the potential slip plane, σ_n, and the cohesion (C) of the material according to the formula

$$\tau_s = \sigma_n \tan\theta + C, \tag{23}$$

where θ is the angle of internal friction. In this equation τ_s, the shear strength, signifies the value of resolved shear along the slip plane that will lead to failure across the plane (Scholz 2002). Bruno & Bovberg (1992) give Mohr envelope failure values of $\theta = 12^o$ and $C = 1.6$ MPa for the siltstones of the San Joaquin unit [see also Fossum & Fredrich (2000)], the formation where the failure
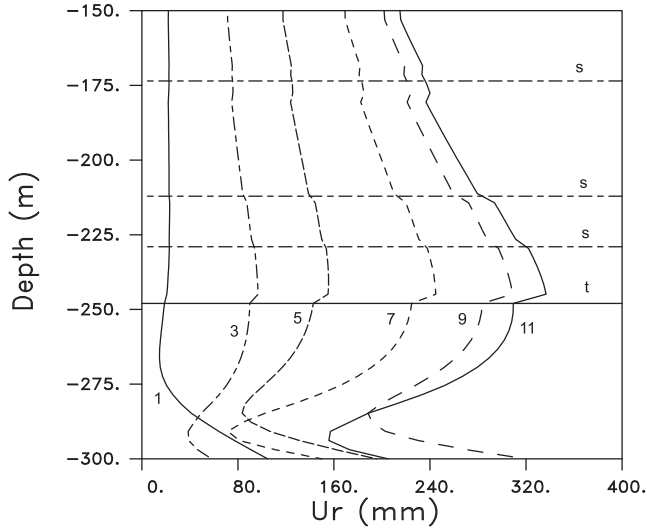
Figure 18. Radial displacement magnitude as a function of depth from a caliper log in the well indicated by the open circle in Fig. 3. The six curves correspond to different time intervals and the labelled values indicate the number of months since the well was completed. The dashed horizontal lines denote shear zones (s) determined by the multifinger caliper log. The solid horizontal line corresponds to the depth of a tagged zone (t) beyond which the well was impassable.

occurred. Because the failure occurred on a sub-horizontal bedding plane the normal stress is the vertical stress σ_{zz} which we assume is due to the weight of the overlying sediments, 4.5 MPa, plus the vertical stress changes due to production and injection. We have not accounted for the contribution of the production-induced stress changes prior to the drilling of the well. However, from our inversions of the entire InSAR range change data set we have found that the monthly variations are in the range of 0.5 MPa. We have plotted the right-hand-side of eq. (23), with the parameters from Bruno & Bovberg (1992) and using our vertical stress changes, as the solid sub-horizontal curve in Fig. 19. While there are muted tem-

poral variations, the curve is generally horizontal, signifying that the monthly vertical stress changes due to injection and production are not significantly altering the estimated shear strength over time. In Fig. 19, we see that the horizontal shear stresses σ_{xz} and σ_{yz} are increasing roughly linearly with time. Thus, the resolved peak horizontal stress is also increasing with time and reaches and exceeds the estimated shear strength of the formation near the beginning of 2012. This is in accordance with the failure of the well in early 2012, as indicated by the solid vertical line if Fig. 19.

The second yield condition is a Drucker–Prager failure criteria of the form

$$\sqrt{J_2} = A + BI_1 \tag{24}$$

where I_1 is the first invariant (trace) of the Cauchy stress tensor given by

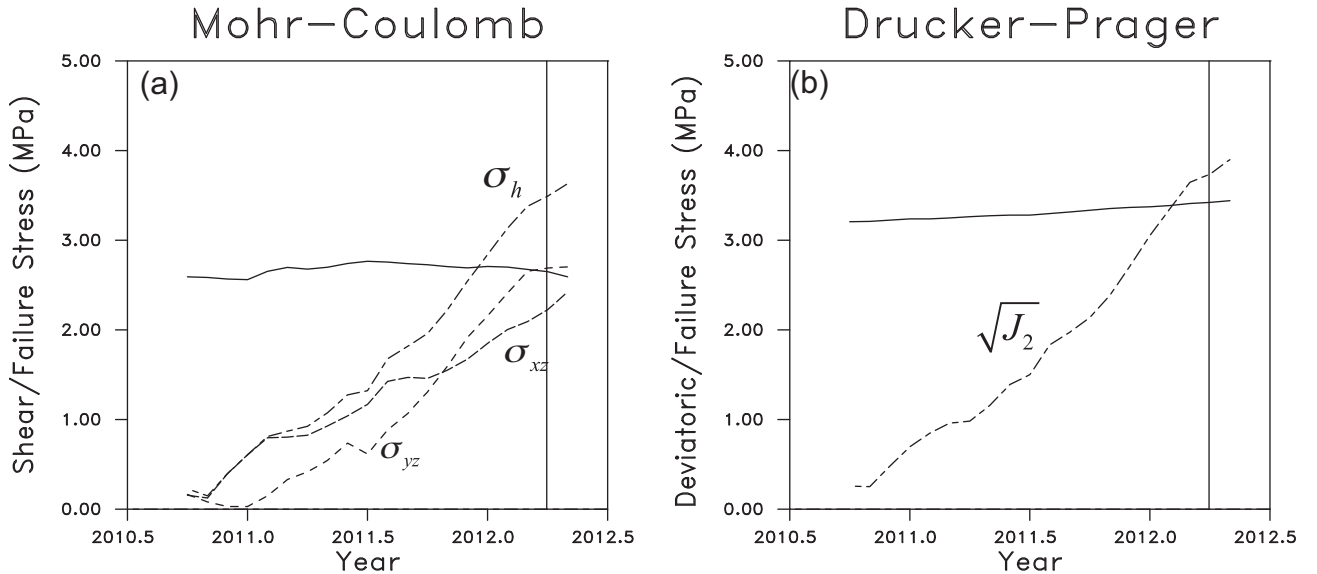$$I_1 = \sigma_{11} + \sigma_{22} + \sigma_{33} \tag{25}$$

and J_2 is the second invariant of the deviatoric part of the Cauchy stress tensor given by

$$J_2 = \frac{1}{2} D_{ij} D_{ij} \tag{26}$$

where

$$D_{ij} = \sigma_{ij} - \frac{1}{3} \delta_{ij} \sigma_{kk}. \tag{27}$$

The diagonal elements of the stress tensor σ_{11}, σ_{22} and σ_{33} correspond to σ_{xx}, σ_{yy} and σ_{zz}, respectively, and similarly for the off-diagonal elements. The criterion (24) was introduced to treat the plastic deformation and failure of soils and other pressure-dependent materials (Drucker & Prager 1952). The values of the coefficients are $A = 1.88$ MPa and $B = 0.09$ (Bruno & Bovberg 1992; Fossum & Fredrich 2000). We assume that the initial stress field is just due to the weight of the overlying sediments, neglecting the unknown initial horizontal tectonic stresses. The field operator noted that that the local stresses have been significantly altered by the injection and production activities and that there no longer appears to be a systematic direction of failure in the field. Thus, the horizontal

Figure 19. Left panel: a Mohr–Coulomb failure condition (subhorizontal solid line) indicating the shear strength of the overburden in the San Joaquin formation. The dashed lines are the horizontal shear stress σ_h, and the two components of horizontal shear stress (σ_{xz} and σ_{yz} computed from the estimates of stress change). Right panel: a Drucker–Prager failure criterion (sub-horizontal solid line) and the value of the square root of the second invariant of the deviatoric part of the stress tensor, given by eqs (22) and (23).

stress changes appear to be dominated by the field activities over the time interval of interest. In Fig. 19, we plot the right-hand-side of eq. (24), rhs = 1.88MPa + 0.09I_1 as a solid subhorizontal line. The dashed line, representing $\sqrt{J_2}$, increases almost linearly with time. It intersects the failure line just after the start of 2012, roughly three months before the well fails. Thus, the estimated stress changes and the estimated yield criteria are compatible with the observed well failure.

4 DISCUSSION

The dynamic nature of the stress field, evident in Fig. 17, provides some indication as to why well failures are observed throughout the field and are difficult to predict based upon large scale stress changes. For example, there is little correlation between shear failure in wells and their position with respect to the outer edge of the field, where the large scale and long term horizontal shear stress is often the greatest. This was also the case for the South Belridge Field to the north, where it was observed that well failures occurred throughout the area of production rather than simply along the perimeter or within the centre of the zone of subsidence (Hansen *et al.* 1995; Myer *et al.* 1996; Fredrich *et al.* 2000). Furthermore, an analysis of the spatial distribution of well failures at the South Belridge field, obtained from a comprehensive database, indicates that well damage is influenced by local patterns of injection and production (Fredrich *et al.* 2000). High-resolution estimates, obtained frequently in time, may present an opportunity to improve upon this last observation. Specifically, we can examine how the changes in the components of the stress tensor correlate with well failures. Unfortunately, the time at which a well fails is not accurately known in this field because it can be a number of months before the failure is detected. However, during 2012 the condition of all existing wells in the field was determined. Taking advantage of this information, we examined all wells that were drilled between the beginning of 2010 and the end of 2012. Next, we calculated the fraction of wells that failed in each of the 100 m by 100 m grid blocks used in our partitioning of the field (see Fig. 4). The failed wells in the grid blocks were then correlated with the peak of each stress component attained between 2010 and 2012 in the grid block. The components of stress change were estimated for a depth of 200 m, where most well failures occur. The number of failed wells correlates most strongly with the stress component σ_{zz} (Fig. 20). Because we are considering peak magnitudes, rather than signed values, there is a positive correlation. The next highest correlation is between failed wells and the two horizontal stress components σ_{xz} and σ_{yz}. These correlations are supportive of the Mohr–Coulomb yield condition (23) for a horizontal or subhorizontal failure surface. In that case, σ_{zz} may be associated with the normal stress on the plane, σ_n, and σ_{xz} and σ_{yz} are the shear stresses acting to cause slip on the plane. Therefore, changes in these stress components might be expected to lead to well failures.

5 CONCLUSIONS

Observed surface deformation, coupled with information on fluid volume fluxes and elastic parameters, can provided high-resolution estimates of stress changes associated with injection and production. Our results indicate that stress changes at depth can vary rapidly in both space and time due to the proximity to the injection and production wells. The rapid spatial variations may not be reflected in observed surface deformation, due to the smoothing of the dis-
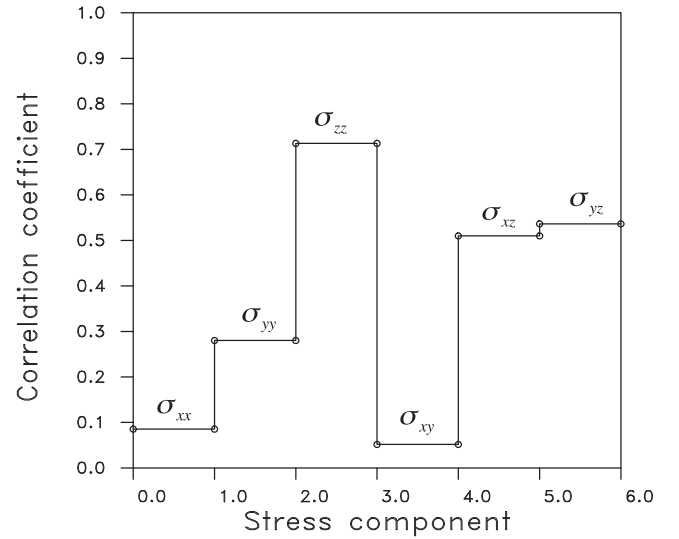
Figure 20. Coefficients indicating the correlation between the peak values of the estimated stress components in each grid block at 200 m and the percentage of failed wells in that grid block.

placement field with distance from the source. The intricate pattern of stress variations, with large stresses located throughout the overburden, may explain why well failures often occur throughout a deforming reservoir and are not concentrated around the rim of a surface subsidence bowl.

The results also highlight the non-uniqueness inherent in the interpretation of surface geodetic data. While we cannot eliminate such non-uniqueness, as it is a fundamental limitation of the data, constraining the inversion to honour a given set of production and injection data does provide an interesting solution, one that may better reflect the spatial variation of volume change within the reservoir. However, such constraints or penalty terms can introduce their own set of errors, for example if the fluid fluxes are not measured accurately, and the quality of the inversion may be impacted. One way to reduce the non-uniqueness would be to combine several techniques, such as borehole stress measurements, seismic anisotropy observations, and seismic source mechanisms with our approach. The advantages of geodetic data, its dense spatial coverage and excellent temporal sampling, could overcome some of the limitations of seismic source inversions which depend upon natural seismic events for sampling in space and time. Time-lapse seismic strains, are one data set that can provide improved spatial resolution, because it is possible to estimate strains within a volume of the Earth (Rickett *et al.* 2007). Such data sets also extend the applicability of the method to offshore areas, as do observations from deep-sea pressure sensors (Chadwick *et al.* 2006).

Estimates based upon a layered elastic model, a single layer over a half-space model, and an anticlinal model produce roughly similar solutions for the stress changes, suggesting that the general pattern of stress change can be recovered in the absence of significant lateral heterogeneity. The estimated stress changes depend strongly on the spatial variations in the mechanical properties of the medium. Furthermore, the magnitude of the stress estimates are strongly influenced by the variations in properties with depth. Any deviations from elasticity could be incorporated into more general viscoelastic or elastoplastic models of the overburden. As a first step, one can incorporate elastic coefficients that vary as the material is stressed, allowing for the evolution of the properties of the overburden as it deforms.

ACKNOWLEDGEMENTS

REFERENCES

Aki, K. & Richards, P.G., 1980. *Quantitative Seismology,* Freeman and Sons.

Angelier, J., 2002. Inversion of earthquake focal mechanisms to seismo-tectonic stress IV: a new method free of choice among nodal planes, *Geophys. J. Int.,* **150,** 588–609.

Arnold, R. & Townend, J., 2007. A Bayesian approach to estimating tectonic stress from seismological data, *Geophys. J. Int.,* **170,** 1336–1356.

Aster, R.C., Borchers, B. & Thurber, C.H., 2013. *Parameter Estimation and Inverse Problems,* Elsevier.

Backus, G. & Gilbert, F., 1968. The resolving power of gross earth data, *Geophys. J. R. astr. Soc.,* **16,** 169–205.

Bakulin, V. & Protosenya, A., 1982. Nonlinear effects in travel of elastic waves through rocks, *Proc. USSR Acad. Sci.,* **263,** 214–316 (in Russian).

Bowersox, J.R. & Shore, R.A., 1990. Reservoir compaction of the Belridge diatomite and surface subsidence, South Belridge field, Kern County, California, in *Structure, Stratigraphy, and Hydrocarbon Occurrence of the San Joaquin Basin, California,* eds Knespert, J.G. & Reid, S.A., Pacific Section of the SEPM and AAPG.

Bruno, M.S. & Bovberg, C.A., 1992. Reservoir compaction and surface subsidence above the Lost Hills Field, California, in *Rock Mechanics Proceedings of the 33rd U.S. Symposium,* pp. 263–272, eds Tillerson, J.R. & Wawersik, W.R., A.A. Balkema.

Chadwick, W.W., Nooner, S.L., Zumberge, M.A., Embley, R. & Fox, C.G., 2006. Vertical deformation monitoring at Axial Seamount since its 1998 eruption using deep-sea pressure sensors, *J. Volcanol. Geotherm. Res.,* **150,** 313–327.

Crampin, S., 1978. Seismic wave propagation through a cracked solid: polarization as a possible dilatancy diagnostic, *Geophys. J. R. astr. Soc.,* **53,** 467–496.

De Rouffignac, E. & Bondor, P.L., 1995. Land subsidence and well failure in the Belridge diatomite oil field, Kern County, California. Part I. Experiments, model and verification, in *Land Subsidence, Proceedings of the Fifth International Symposium on Land Subsidence,* IAHS Publication 234, The Hague.

Dietrich, J.K. & Scott, J.D., 2007. Modeling thermally induced compaction in diatomite, *Soc. Pet. Eng. J.,* **12,** 130–144.

Drucker, D.C. & Prager, W., 1952. Soil mechanics and plastic analysis for limit design, *Q. Appl. Math.,* **10,** 157–165.

Farley, T., 1990. Heavy oil reservoirs in the Tulare fold belt, Cymric-McKittrick fields Kern County, California, in *Structure, Stratigraphy, and Hydrocarbon Occurrences of the San Joaquiv Basin, California,* pp. 181–203, AAPG Search and Discovery Article 91003, AAPG Annual Convention, San Francisco, California.

Ferretti, A., 2014. *Satellite InSAR Data: Reservoir Monitoring from Space,* European Association of Geoscientists and Engineers.

Ferretti, A., Prati, C. & Rocca, F., 2001. Permanent Scatterers in SAR interferometry, *IEEE Trans. Geosci. Remote Sens.,* **39,** 8–20.

Ferretti, A., Fumagalli, A., Novali, F., Prati, C., Rocca, F. & Rucci, A., 2011. A new algorithm for processing interferometric data-stacks: SqueeSAR, *IEEE Trans. Geosci. Remote Sens.,* **49,** 3460–3470.

Fielding, E.J., Blom, R.G. & Goldstein, R.M., 1998. Rapid subsidence over oil fields measured by SAR interferometry, *Geophys. Res. Lett.,* **25,** 3215–3218.

Fossum, A.F. & Fredrich, J.T., 1998, *Estimation of Constitutive Parameters for the Belridge diatomite, South Belridge, Diatomite field, Sandia Report,* SAND98-1407, Albuquerque, New Mexico.

Fossum, A.F. & Fredrich, J.T., 2000, *Constitutive Models for the Etchegoin Sands, Belridge Diatomite, and Overburden Formations at the Lost Hills Oil Field, California, Sandia Report, SAND98-0827,* Albuquerque, New Mexico.

Fredrich, J.T., Arguello, J.G., Deitrick, G.L. & de Rouffignac, E.P., 2000. Geomechanical modeling of reservoir compaction, surface subsidence, and casing damage at the Belridge diatomite field, *Soc. Pet. Eng.,* **3,** 348–359.

Fung, Y.C., 1969. *A First Course in Continuum Mechanics,* Prentice-Hall.

Gassmann, F., 1951. Ueber die elastizitat poroser medien, Vierteljahrsschrift der Naturforschenden Gesellschaft in Zurich, Heft, **1**.

Gephart, J.W. & Forsyth, D.W., 1984. An improved method for determining the regional stress tensor using earthquake focal mechanism data: application to the San Fernando earthquake sequence, *J. geophys. Res.,* **89,** 9305–9320.

Gurevich, B., Pervukhina, M. & Makarynska, D., 2011. An analytic model for the stress-induced anisotropy of dry rocks, *Geophysics,* **76,** WA125–WA133.

Hager, B.H. & Clayton, R.W., 1989. Constraints on the structure of mantle convection using seismic observations, flow models, and the geoid, in *Mantle Convention, Plate Tectonics, and Global Dynamics,* ed. Peltier, R.W., Gordon and Breach Science Publishers.

Hansen, K.S., Prats, M. & Chan, C.K., 1995. Modeling reservoir compaction and surface subsidence at South Belridge, *SPE Prod. Facil.,* **10,** 134–143.

Hanssen, R., 2001. *Radar Interferometry: Data Interpretation and Error Analysis,* Kluwer.

Hardebeck, J.L. & Hauksson, E., 2001. Stress orientation obtained from earthquake focal mechanisms: what are appropriate uncertainty estimates?, *Bull. seism. Soc. Am.,* **91,** 250–262.

Hardebeck, J.L. & Michael, A.J., 2006. Damped regional-scale stress inversions: methodology and examples for southern California and the Coalinga aftershock sequences, *J. geophys. Res.,* **111,** 1–11.

Humphreys, E. & Clayton, R.W., 1988. Adaptation of back projection tomography to seismic travel time problems, *J. geophys. Res.,* **93,** 1073–1085.

Inoue, H., Fukao, Y., Tanabe, K. & Ogata, Y., 1990. Whole mantle P-wave travel time tomography, *Phys. Earth planet. Inter.,* **59,** 294–328.

Jackson, D.D., 1979. The use of a priori data to resolve non-uniqueness in linear inversion, *Geophys. J. R. astr. Soc.,* **57,** 137–157.

Johnson, P.A. & Rasolofosaon, P.N.J., 1996. Nonlinear elasticity and stress-induced anisotropy in rock, *J. geophys. Res.,* **101,** 3113–3124.

Kennett, B.L.N., 1983. *Seismic Wave Propagation in Stratified Media,* Cambridge Univ. Press.

Kumar, M. & Beatty, F.D. 1995. Cyclic steaming in heavy oil diatomite, in *Western Regional Meeting of the Society of Petroleum Engineers*, Bakersfield, CA, 8-10 March, 1995, SPE29623, 109–122.

Leary, P.C., Crampin, S. & McEvilly, T.V., 1990. Seismic fracture anisotropy in the Earth's crust, *J. geophys. Res.,* **95,** 11 105–11 114.

Ljunggren, C., Chang, Y., Janson, T. & Christiansson, R., 2003. An overview of rock stress measurement methods, *Int. J. Rock Mech.,* **40,** 975–989.

Mavko, G., Mukerji, T. & Godfrey, N., 1995. Predicting stress-induced velocity anisotropy in rocks, *Geophysics,* **60,** 1081–1087.

Menke, W., 1989. *Geophysical Data Analysis: Discrete Inverse Theory,* Academic Press.

Michael, A.J., 1984. Determination of stress from slip data: faults and folds, *J. geophys. Res.,* **89,** 11 517–11 526.

Miller, D.D. & McPherson, J.G., 1992. South Belridge Field - U.S.A. San Joaquin Basin, California, in *Structural Traps VII,* pp. 221–244, AAPG Special Volumes, American Association of Petroleum Geologists.

Mount, V.S. & Suppe, J., 1987. State of stress near the San Andreas fault: implications for wrench tectonics, *Geology,* **15,** 1143–1146.

Myer, L., Jacobsen, J., Horsman, J., Fredrich, J.T., Wawersik, W., Arguello, J.G., Bruno, M. & Qian, H., 1996. Use of visualization techniques in analysis of well failures in diatomite reservoirs, *Leading Edge,* **15,** 185–189.

Noble, B. & Daniel, J.W., 1977. *Applied Linear Algebra,* Prentice-Hall.

Paige, C.C. & Saunders, M.A., 1982, *LSQR:* An algorithm for sparse linear equations and sparse least squares, *ACM Trans. Math. Softw.,* **8,** 43–71.

Parker, R.L., 1994. *Geophysical Inverse Theory,* Princeton Univ. Press.

Press, W.H., Teukolsky, S.A., Vetterling, W.T. & Flannery, B.P., 2007. *Numerical Recipes,* Cambridge Univ. Press.

Pride, S.R., 2005. Relationships between seismic and hydrological properties, in *Hydrogeophysics,* pp. 235–290, eds Rubin, Y. & Hubbard, S.S.

Prioul, R., Bakulin, A. & Bakulin, V., 2004. Nonlinear rock physics model for estimation of 3D subsurface stress in anisotropic formations: theory and laboratory verification, *Geophysics,* **69,** 415–425.

Pulliam, R.J., Vasco, D.W. & Johnson, L.R., 1993. Tomographic inversions for mantle *P* wave velocity structure based on the minimization of the l^2 and l^1 norms of International Seismological Center travel time residuals, *J. geophys. Res.,* **98,** 699–734.

Rickett, J., Duranti, L., Hudson, L., Regel, T. & Hodgson, N., 2007. 4D time strain and the seismic signature of geomechanical compaction at Genesis, *Leading Edge,* **26**(5), 644–647.

Roscoe, K.H., Schofield, A.N. & Wroth, C.P., 1958. On the yielding of soils, *Geotechnique,* **8,** 22–53.

Sarkar, D., Bakulin, A. & Kranz, R.L., 2003. Anisotropic inversion of seismic data for stressed media: theory and a physical modeling study on Brea Sandstone, *Geophysics,* **68,** 1–15.

Sandler, I.S. & Rubin, D., 1979. An algorithm and a modular subroutine for the cap model, *Int. J. Numer. Anal. Methods Geomech.,* **3,** 173–186.

Scholz, C.H., 2002. *The Mechanics of Earthquakes and Faulting,* Cambridge Univ. Press.

Shapiro, S.A. & Kaselow, A., 2005. Porosity and elastic anisotropy of rocks under tectonic stress and pore-pressure changes, *Geophysics,* **70,** N27–N38.

Sinha, B.K. & Kostek, S., 1996. Stress-induced azimuthal anisotropy in borehole flexural waves, *Geophysics,* **61,** 1899–1907.

Skempton, A.W., 1954. The pore-pressure coefficients A and B, *Geotechnique,* **4,** 143–147.

Stakgold, I., 1979. *Green's Functions and Boundary Value Problems,* John Wiley and Sons.

Stosur, J.J. & David, A., 1976. Petrophysical evaluation of the diatomite formation of the Lost Hills Field, California, *J. Pet. Technol.,* **28,** 1138–1144.

Strickland, F.G., 1985. Reasons for production decline in the diatomite, Belridge Oil Field: a rock mechanics view, *J. Pet. Technol.,* **37,** 521–526.

Tarantola, A., 2005. *Inverse Problem Theory,* SIAM.

Terakawa, T. & Matsu'ura, M., 2008. CMT data inversion using a Bayesian information criterion to estimate seismogenic stress fields, *Geophys. J. Int.,* **172,** 674–685.

Thurston, R.N. & Brugger, K., 1964. Third-order elastic constants and the velocity of small amplitude elastic waves in homogeneously stressed media, *Phys. Rev.,* **133**(6A), A1604–A1610.

Vasco, D.W. & Datta-Gupta, A., 2016. *Subsurface Fluid Flow and Imaging,* Cambridge Univ. Press.

Vasco, D.W. & Johnson, L.R., 2003. Resolution, uncertainty, and whole Earth tomography, *J. geophys. Res.,* **108,** 1–26.

Vasco, D.W. & Ferretti, A., 2005. On the use of quasi-static deformation to understand reservoir fluid flow, *Geophysics,* **70,** O13–O27.

Vasco, D.W., Johnson, L.R. & Goldstein, N.E., 1988. Using surface deformation and strain observations to determine deformation at depth, with and application to Long Valley Caldera, California, *J. geophys. Res.,* **93,** 3232–3242.

Vasco, D.W., Pulliam, R.J. & Johnson, L.R., 1993. Formal inversion of ISC arrival times for mantle P-velocity structure, *Geophys. J. Int.,* **113,** 586–606.

Vasco, D.W., Johnson, L.R. & Marques, O., 1999. Global Earth structure: inference and assessment, *Geophys. J. Int.,* **137,** 381–407.

Vasco, D.W., Karasaki, K. & Doughty, C., 2000. Using surface deformation to image reservoir dynamics, *Geophysics,* **65,** 132–147.

Vasco, D.W., Wicks, C., Karasaki, K. & Marques, O., 2002a. Geodetic imaging: reservoir monitoring using satellite interferometry, *Geophys. J. Int.,* **149,** 555–571.

Vasco, D.W., Karasaki, K. & Nakagome, O., 2002b. Monitoring production using surface deformation: the Hijiori test site and the Okuaizu geothermal field, Japan, *Geothermics,* **31,** 303–342.

Vasco, D.W., Rucci, A., Ferretti, A., Novali, F., Bissell, R., Ringrose, P., Mathieson, A. & Wright, I., 2010. Satellite-based measurements of surface deformation reveal fluid flow associated with the geological storage of carbon dioxide, *Geophys. Res. Lett.,* **37,** doi:10.1029/2009GL041544, 1–5.

Wang, H.F., 2000. *Theory of Linear Poroelasticity with Applications to Geomechanics and Hydrogeology,* Princeton Univ. Press.

Wang, L., Hainzi, S. & Mai, P.M., 2015. Quantifying slip balance in the earthquake cycle: coseismic slip model constrained by interseismic coupling, *J. geophys. Res.,* **120,** 8383–8403.

Wang, R., Lorenzo-Martin, F. & Roth, F., 2003. Computation of deformation induced by earthquakes in a multilayered elastic crust - FORTRAN programs EDGRN/EDCMP, *Comput. Geosci.,* **29,** 195–207.

Wang, R., Lorenzo-Martin, F. & Roth, F., 2006. PSGRN/PSCMP - a new code for calculating co- and post-seismic deformation, geoid and gravity changes base on the viscoelastic-gravitational dislocation theory, *Comput. Geosci.,* **32,** 527–541.

Zang, A. & Stephansson, O., 2010. *Stress Field of the Earth's Crust,* Springer.

APPENDIX: RELATING GRID BLOCK VOLUME CHANGE TO INJECTED AND PRODUCED FLUID VOLUMES

Given the volumes of the various fluids, say ΔV_{q_i} where $i = 1, 2, \ldots, N_f$ for N_f fluids, introduced or removed from a given grid block we wish to estimate its fractional volume change. Needless to say, this is a rather complicated task that will depend strongly on the behaviour of the medium. Here, we will assume that the grid block as a whole can be modelled as a poroelastic body for a specified time interval. In our application the time intervals are generally one month. This appendix provides an illustration of the considerations that enter into the scaling between fluid and grid block volume changes. The results will provide a range of values for the scaling factor when the medium behaves poroelastically.

We shall be modelling cyclic steam injection in which the duration of the cycles is short compared to the lifetime of the well. Therefore, a given well will be subject to tens to hundreds of cycles. Typically, in a given time interval, very few wells will be undergoing their first initial injection in which the rock is fractured and the surrounding regions is subject to significant heating. Therefore, we shall ignore the transient effects due to the initiation of cyclic steaming. Such effects include the temperature change around the fracture and associated expansion as well as the porosity changes due to the initiation of the fracture.

For simplicity, consider the effect of a net fluid volume change dV_q. For a grid block that behaves in a poroelastic fashion, the change in confining pressure P_c and fluid pressure P_f are linearly related to the change in grid block volume dV and fluid volume dV_q according to

$$dP_c = -K_u \frac{dV}{V} + \alpha M \frac{dV_q}{V} \tag{A1}$$

$$dP_f = -\alpha M \frac{dV}{V} + M \frac{dV_q}{V} \tag{A2}$$

$$d\phi = -\left[\frac{(1-\phi)}{K_d} - \frac{1}{K_s}\right](dP_c - dP_f) \tag{A3}$$

where K_d and K_u are the drained and undrained bulk modulus, respectively (Wang 2000). In the undrained state, the fluid content is constant and there is no fluid transfer into or out of the sample. Drained moduli correspond to experiments in which fluid may freely enter and exit a sample, but the pressure is held constant.

The fluid storage coefficient M represents the amount of fluid that can accumulate in a sample at constant volume. The quantity α is the Biot-Willis coefficient, representing the ratio of added fluid volume to the change in bulk volume at constant pressure. A good discussion of these various poroelastic parameters may be found in Wang (2000), Pride (2005, p. 264), and Vasco & Datta-Gupta (2016, p. 92).

Because we are considering times after the initiation of injection and fracture formation, we shall assume that the porosity change associated with the injection may be neglected so that $d\phi = 0$. From eq. (A3) we see that $dP_c = dP_f$ and we may equate the right-hand-sides of equations (A1) and (A2)

$$(K_u - \alpha M) \frac{dV}{V} = M(1-\alpha) \frac{dV_q}{V}. \tag{A4}$$

The undrained bulk modulus K_u may be written in terms of α, M, and Skemptons coefficient B,

$$K_u = \frac{\alpha M}{B} \tag{A5}$$

where Skemptons coefficient is the ratio of pore pressure to confining pressure under undrained conditions (Skempton 1954). Substituting for K_u in eq. (A4) gives

$$\left(\frac{\alpha}{B} - \alpha\right) \frac{dV}{V} = (1-\alpha) \frac{dV_q}{V}. \tag{A6}$$

In order to express the parameters in this equation in terms of the bulk moduli of the drained rock (K_d), the composite fluid (K_f), and the solid grains (K_s), we invoke Gassmann's eq. (Gassmann 1951) which allows us to write the coefficient on the left-hand side as

$$\frac{\alpha}{B} - \alpha = \phi \left(\frac{K_d}{K_f} - \frac{K_d}{K_s}\right). \tag{A7}$$

Furthermore, one can write α in terms of K_d and K_s

$$\alpha = 1 - \frac{K_d}{K_s} \tag{A8}$$

and eq. (A6) becomes

$$\phi \left(\frac{1}{K_f} - \frac{1}{K_s}\right) \frac{dV}{V} = \frac{1}{K_s} \frac{dV_q}{V} \tag{A9}$$

or

$$\frac{dV}{V} = \frac{K_f}{\phi (K_s - K_f)} \frac{dV_q}{V}. \tag{A10}$$

One can carry out the derivation for multiple fluids, generalizing eqs (A1) and (A2) to allow for fluids with different properties. For example, in the field application there are at least four fluid phases, water, oil, gas, and steam. For N_f fluids where the ith fluid is characterized by the bulk modulus K_i, we can carry the derivation through to the final equation

$$\frac{dV}{V} = \sum_{i=1}^{N_f} \frac{K_i}{\phi (K_s - K_i)} \frac{dV_{q_i}}{V}. \tag{A11}$$

The relationship (A10) may be used to estimate a range of scaling factors relating the net fluid volume change to the fractional volume change of the appropriate grid block. Because the fluid flux is dominated by the aqueous phase, the injected steam quickly condenses to water, and the bulk modulus of water is the largest, we will assume the $K_f = 2$ GPa, that of water. Diatomite is a silica-based rock so for the solid grains we shall use the bulk modulus of quartz, $K_s = 40$ GPa. There is considerable uncertainty in the value of porosity that we should use in the calculations. The porosity of diatomite is quite high, exceeding 60 per cent in many instances. However, the permeability is quite low and much of the pore space is inaccessible. Most of the fluid flow probably takes place within the natural and induced fractures in the diatomite. Thus, the porosity could be as low as a few percent, depending on the nature of the fractures. If we allow for porosity variations between 5 per cent and 60 per cent, a water-rich fluid, and a silica-based rock then eq. (A10) predicts scaling factors between 0.1 and 1.